

Freed from Iron: easy release of a stable ketene from the reaction of CO with di-iron bis- μ^2 -alkylidenes.

Sandip Munshi,^{1,a} Raphaël Ravel-Massol,^{1,a} Ricardo Garcia-Serres,^b Nicolas Suaud,^c Rémi Maurice,^d Nathalie Saffon-Merceron,^e Nicolas Mézailles,^{a*} Marie Fustier-Boutignon.^{a*}

Table of content

1. Experimental details.....	1
a. Reagent and solvents	1
b. Apparatus	2
2. Synthesis.....	4
a. Synthesis of 3 (μ^2 -SCS)Fe ₂ (CO) ₆	4
b. Synthesis of 4	4
c. Reaction between 2 and CO.....	5
3. NMR characterisation.....	6
a. NMR spectra for compound 3 (μ^2 -SCS)Fe ₂ (CO) ₆	6
b. NMR spectra for compound 4	10
c. NMR data for intermediate A at -40°C.....	13
4. IR spectroscopy	15
a. IR spectra of 3 and 4	16
Circles represents absorption from impurities.	16
b. IR spectrum of the byproduct of the reaction between 3 and CO.....	16
5. Mass spectroscopy	17
a. Compound 4	17
b. Byproduct of the reaction of 2 and CO.	18
6. X-ray diffraction.....	20
7. Mössbauer spectroscopy.....	23
8. Computational details	25
9. References.....	28

1. Experimental details
 - a. Reagent and solvents

All the reactions were carried out in a M-Braun glove box or using standard Schlenk techniques under N₂ or Ar. Commercial compounds stored under N₂ or Ar were used directly without any further purification, otherwise products were degassed before use. All solvents were taken from MBSPS-800 solvent purification system, degassed by three freeze-thaw-pump cycles and

stored over freshly activated molecular sieves under N₂ or Ar. Compound **1**, **2** and **3** were synthesised following previously reported procedure.¹

b. Apparatus

¹H, ³¹P, ¹³C, and ¹⁹F NMR spectra were recorded on Bruker Avance 300, 400, 500 and 600 MHz spectrometers. ¹H and ¹³C chemical shifts reported are referenced internally to residual proton (¹H) and deuterated (¹³C) solvent, while ³¹P chemical shifts are referenced to an external standard of phosphoric acid.

High resolution mass spectra (Electrospray) were obtained with Xevo G2 Q TOF (Waters) mass spectrometers and GCT Premier (Waters) (DCI-CH₄).

Gas chromatography (CO₂ detection) was performed using a GC Perkin Elmer Clarus 590, equipped with a Elite PLOT Q column (30m 0,53mm, 25mm) and a TCD detector. N₂ was used as a carrier gas, with a flow rate of 9.5 mL/min. Analysis was performed at 50°C in isotherm mode. 150 µL of headspace gas were injected. CO₂ retention time was 1.85 min.

All the electrochemical measurements have been carried out in a nitrogen filled glove-box using µ-Autolab potentiostat (Metrohm, type PGSTAT204) using the NOVA software. Glassy carbon electrode was the working electrode, platinum wire was the counter-electrode, Ag/AgCl was the reference electrode and (Bu₄N)PF₆ was used as the supporting electrolyte. Ferrocene was added after each experiment for calibration.

IR spectra were collected on Thermoscientific Nicolet IS50 - ATR diamond spectrometer equipped with DLATGS detector (4 cm⁻¹ resolution, 32 background scans).

Single-Crystal X-Ray Diffraction:

The crystal data of compounds **3** and **4** were collected using MoK α radiation (wavelength=0.71073 Å) on a Bruker-AXS Quazar APEX II diffractometer using a 30W air-cooled microfocus source (ImS) with focusing multilayer optics. Phi and omega- scans were used. Crystals were mounted in inert oil and crystal structure determinations were affected at 193K. The data were integrated with SAINT² and an empirical absorption correction with SADABS was applied.³ The structures were solved using intrinsic phasing method (ShelXT)⁴ and refined using the least-squares method on F2 (ShelXL).⁵ All non-H atoms were refined with anisotropic displacement parameters. The H atoms were refined isotropically at calculated positions using a riding model.

X-ray crystallographic data have been deposited in the Cambridge Crystallographic Data Centre (<http://www.ccdc.cam.ac.uk/>) with reference numbers: CCDC-2424974 (**3**) and CCDC-2424975 (**4**). These data can be obtained free of charge from <https://www.ccdc.cam.ac.uk/structures/> or from the Cambridge Crystallographic Data Centre, 12 Union Road, Cambridge CB2 1EZ, UK; tel: + 44 (0)1223 336408; fax: + 44 (0)1223336033; or e-mail: deposit@ccdc.cam.ac.uk

Samples were ground into fine powders and placed in Delrin containers. Mössbauer spectra were measured on an Oxford Instruments Spectromag 4000 cryostat containing an 8 T split-pair superconducting magnet. The spectrometer was operated in constant acceleration mode

in transmission geometry. The isomer shifts are referenced against a room temperature metallic iron foil. Analysis of the data was performed using the in-house developed Python package easyMoss.⁶

2. Synthesis

a. Synthesis of **3** (μ^2 -SCS)Fe₂(CO)₆

A dichloromethane solution (20mL) of complex **1** (400 mg, 4.0×10^{-4} mol) was degassed in a fisher porter and placed under 6 bar of CO. After 6 hours of reaction the solvent was dried under vacuum and the red solid was solubilized in diethyl ether (15 mL). The red solution was separated from white solid **4** by filtration. Black/red crystals were obtained by diffusing n-pentane into this concentrate diethyl ether solution. Isolated yield: 46%. **4** can also be extracted on silica column in a glove box under inert atmosphere with a mixture of DCM/n-pentane (20:80 ratio) as elution solvent.

¹H NMR (CD₂Cl₂, 600.13 MHz): 7.80 ppm (m, 4H, o-Ph); 7.69 (m, 2H, p-Ph); 7.53 (m, 4H, m-Ph); 7.45 (m, 2H, p-Ph); 7.32 (m, 4H, m-Ph); 7.21 (m, 4Ho-Ph) ppm.

³¹P{¹H} NMR (CD₂Cl₂, 242.9 MHz): 72.1 ppm.

¹³C{¹H} NMR (CD₂Cl₂, 150.92 MHz): 212.2 (br s, CO); 210.1 (br s, CO); 137.2 (d, ²J_{CP}= 69 Hz, i-CPh); 133.6 (s, p-CPh); 133.3 (d, ²J_{CP}= 11 Hz, o-CPh); 132.8 (d, ²J_{CP}= 65 Hz, i-CPh); 132.1 (p-CPh); 130.3 (d, ²J_{CP}= 11 Hz, o-CPh); 129.4 (d, ³J_{CP}=11 Hz, m-CPh); 128.6 (d, ³J_{CP}=12 Hz, m-CPh); 39.2 (d, ³J_{CP}= 22 Hz) ppm.

IR: 3053, 2040, 1991, 1954, 1938, 1584, 1479, 1434, 1307, 1182, 1159, 1096, 1047, 1026, 998, 746, 721, 687, 594, 555, 530, 490 cm⁻¹.

UV-Vis: 513 nm.

EA: C: 51.38 %, H: 3.33 %, N: 0.08 % (Expected: C: 51.27 %, H: 2.78 %, N: 0.00 %).

b. Synthesis of **4**.

After following the synthesis of **3**, the residual solid of filtration is washed with diethyl ether, then solubilized in 5 mL of dichloromethane. Crystals were obtained by slow diffusion of n-pentane in this solution.

¹H NMR (CD₂Cl₂, 600.1 MHz): 7.81 (m, 8H, o-Ph); 7.46 (m, 4H, p-Ph); 7.37 (m, 8H, m-Ph).

³¹P{¹H} NMR (CD₂Cl₂, 242.9 MHz): 38.0 ppm.

¹³C{¹H} NMR (CD₂Cl₂, 150.92 MHz): 170.5 (t, ²J_{PC}= 9 Hz, CCO); 132.6 (br s, p-CPh); 132.5 (m, o-CPh); 131.9 (m, Δ= 50 Hz, ipso-CPh); 128.8 (m, Δ=28 Hz, CPh); 38.1.

IR: 3363, 3053, 2112, 1585, 1479, 1434, 1309, 1262, 1180, 1159, 1097, 997, 742, 716, 686, 660, 638, 568, 547, 525, 503, 489, 473, 440 cm⁻¹.

HRMS (DCI-CH₄, M+H⁺): exp m/z 475.0509 (100.0%); 476.0541 (29.7%); 477.0504 (9.4%); 478.0516 (2.6%). **Found:** 475.0509; 476.0536; 477.0663; 478.0750.

c. Reaction between **2** and CO

A dichloromethane solution (20mL) of complex **2** (200 mg, 1.2×10^{-4} mol) was degassed in a fisher porter and placed under 6 bar of CO. After 12 hours of reaction the solvent was dried under vacuum and the red/brown solid was solubilized in toluene (20 mL). The red solution was then filtered off while a sticky yellow oil remained in the flask, which was further analysed by multinuclear NMR, IR spectroscopy, Mössbauer spectroscopy and Mass spectrometry.

^1H NMR (CD_2Cl_2 , 300.14 MHz): silent.

^1H NMR ($\text{d}^8\text{-THF}$, 300.14 MHz): 7.84 (m, 8H, o-Ph); 7.32 (m, 8H, m-Ph); 7.11 (m, 4H, p-Ph).

$^{31}\text{P}\{^1\text{H}\}$ NMR (CD_2Cl_2 , 121.5 MHz): silent.

$^{31}\text{P}\{^1\text{H}\}$ NMR ($\text{d}^8\text{-THF}$, 121.5 MHz): 37.4 ppm.

^{13}C NMR (CD_2Cl_2 , 150.92 MHz): silent.

^{19}F NMR (CD_2Cl_2 , 282.3 MHz): -131.16 (br s), -161.55 (t, $^3J_{\text{FF}} = 20.4$ Hz), -165.38 (m) ppm ($\text{B}(\text{C}_6\text{F}_5)_4^-$).

IR: 3057, 2133, 2076, 2040, 1984, 1645, 1511, 1461, 1440, 1271, 1191, 1086, 978, 777, 746, 686 cm^{-1} .

HRMS (ESI): observed fragmentations 1035.0384, 586.9745, 502.9898, 449.0711 (see below).

Evan's method was performed on the yellow product in CD_2Cl_2 on a 300.13 MHz spectrometer at 298K. A Δ of 92.86 Hz was found, which confirm the presence of paramagnetic compounds. The value of μ_{eff} could not be determined, the molar mass of the compound remaining unknown.

3. NMR characterisation

a. NMR spectra for compound **3** (μ^2 -SCS)Fe₂(CO)₆

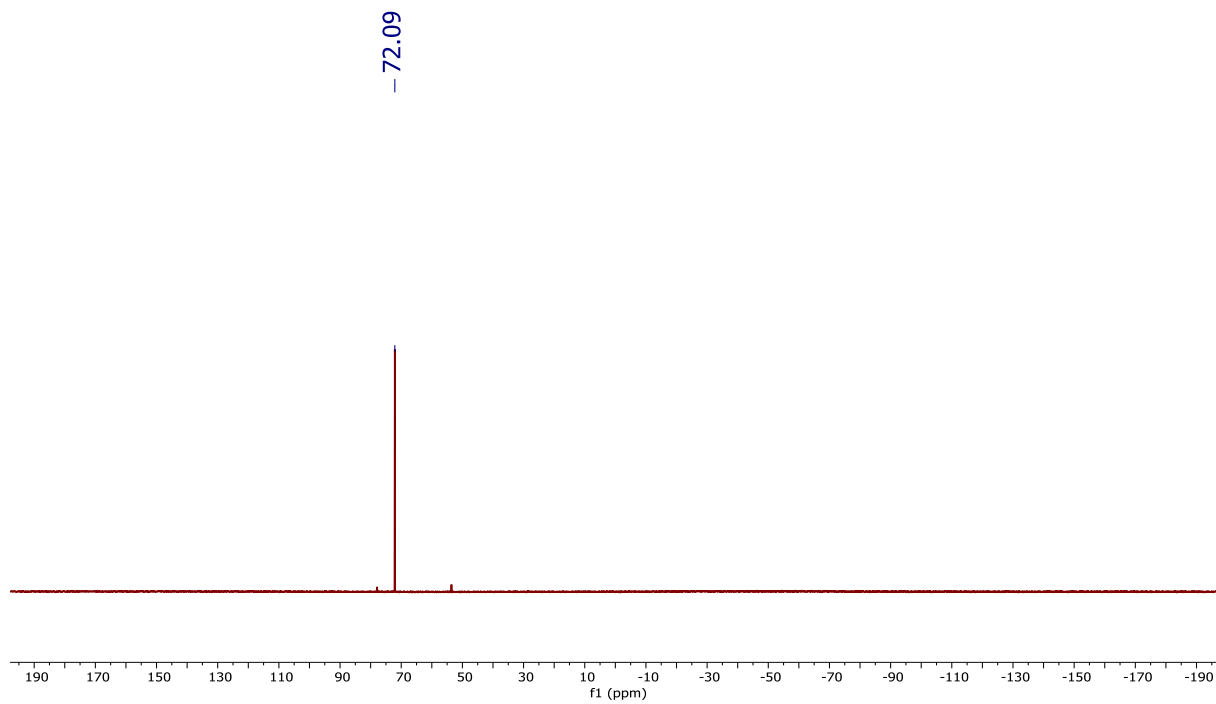


Figure 1: $^{31}\text{P}\{^1\text{H}\}$ NMR of **3** in CD_2Cl_2 .

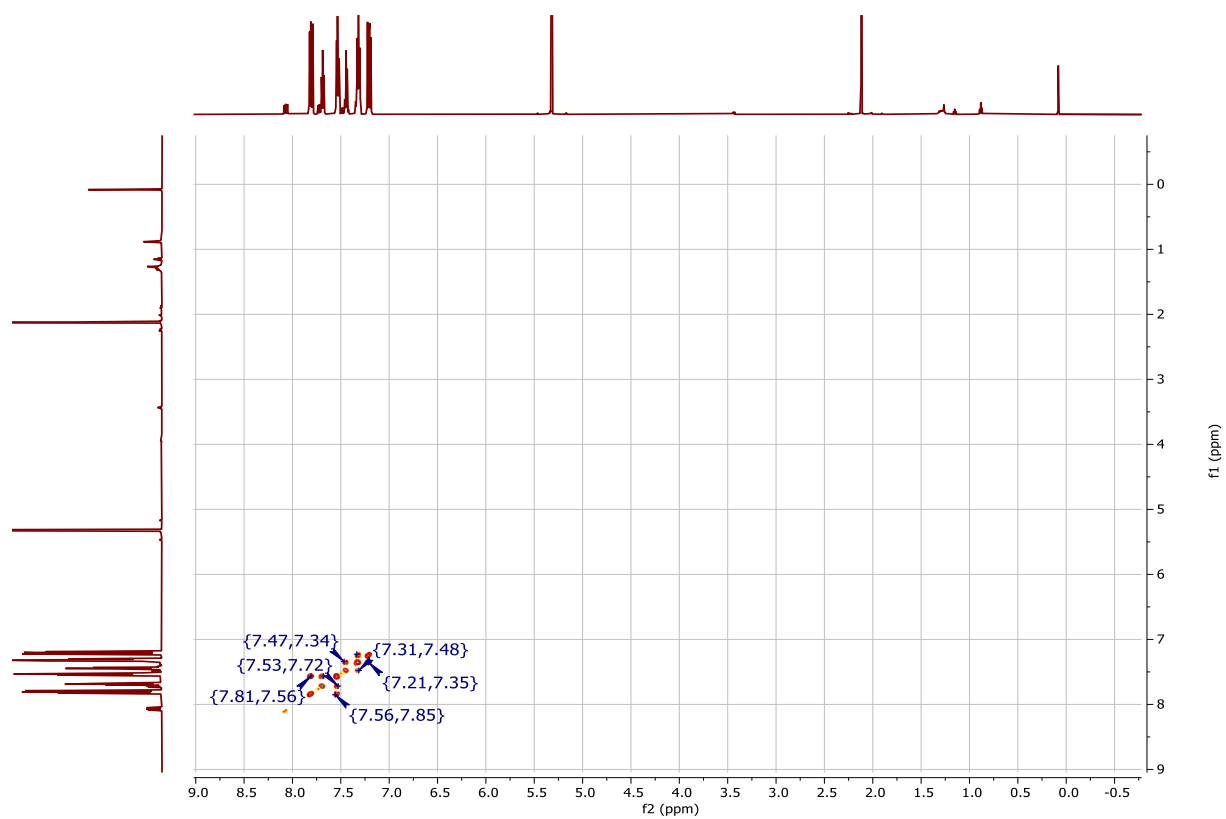


Figure 4: COSY ^1H - ^1H of **3** in CD_2Cl_2 .

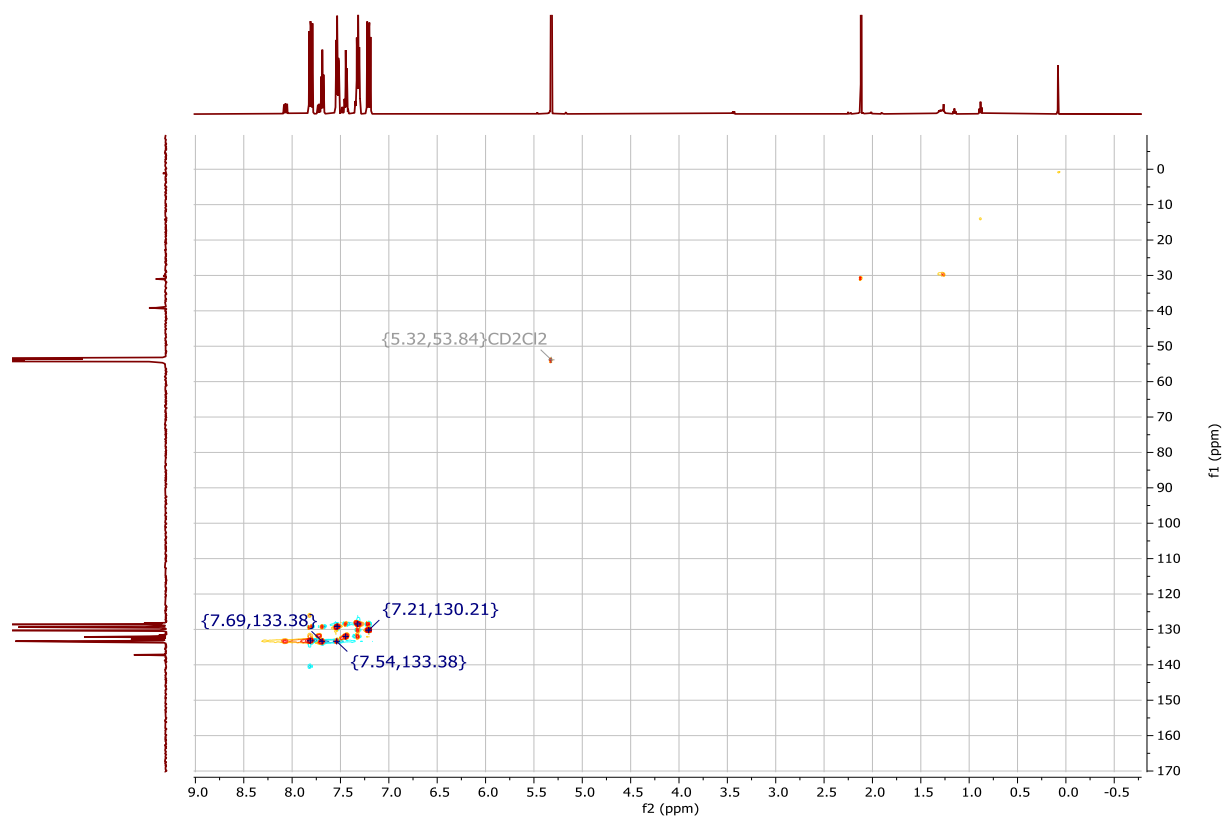


Figure 5: ^{13}C - ^1H HSQC spectrum of **3** in CD_2Cl_2 .

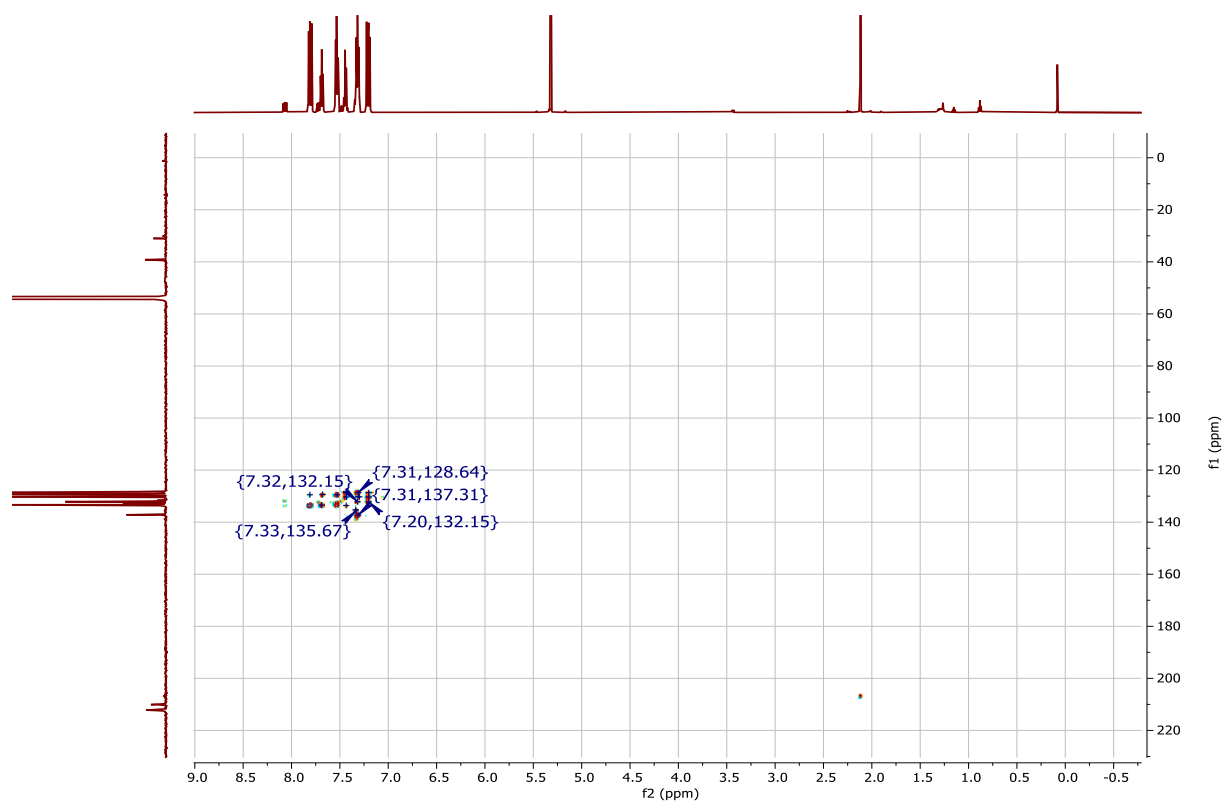


Figure 6: ^{13}C - ^1H HMBC spectrum of **3** in CD_2Cl_2 .

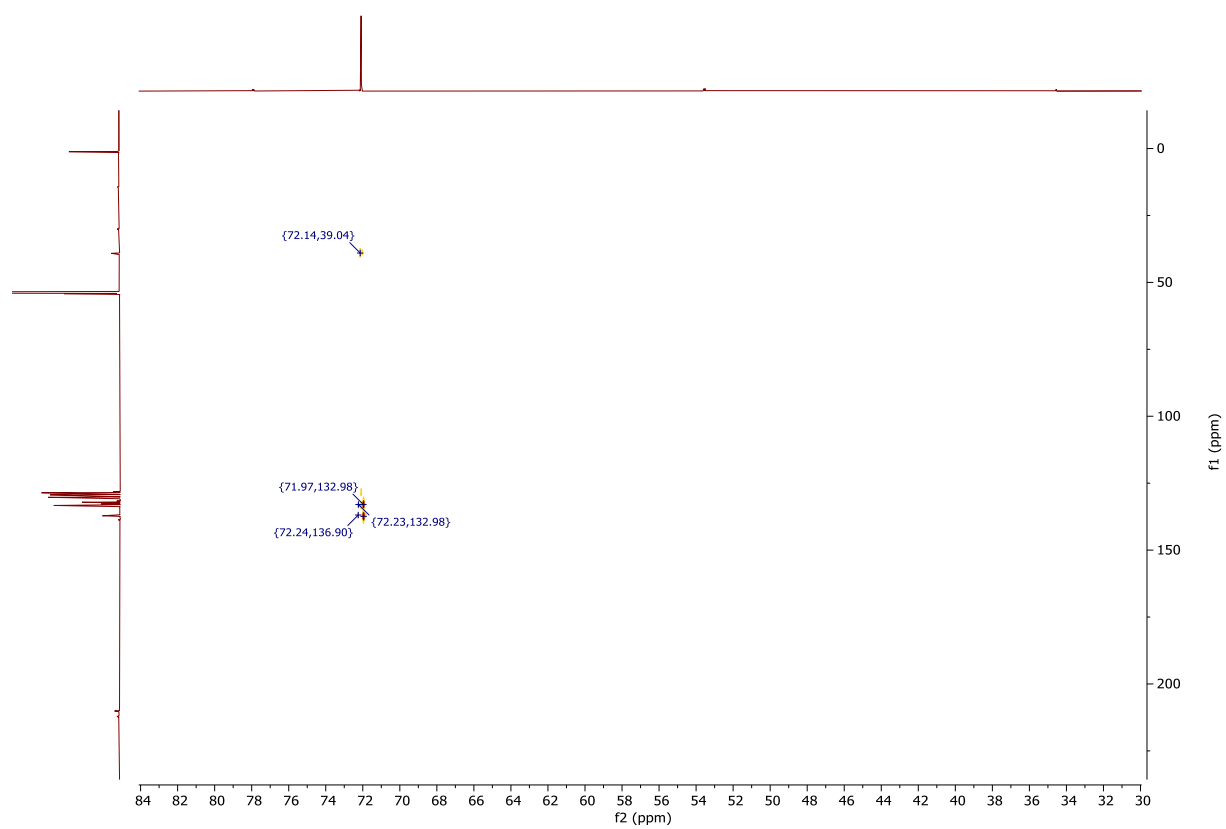


Figure 7: HMBC ^{31}P - $^{13}\text{C}\{^1\text{H}\}$ (80 Hz) of compound **3**.

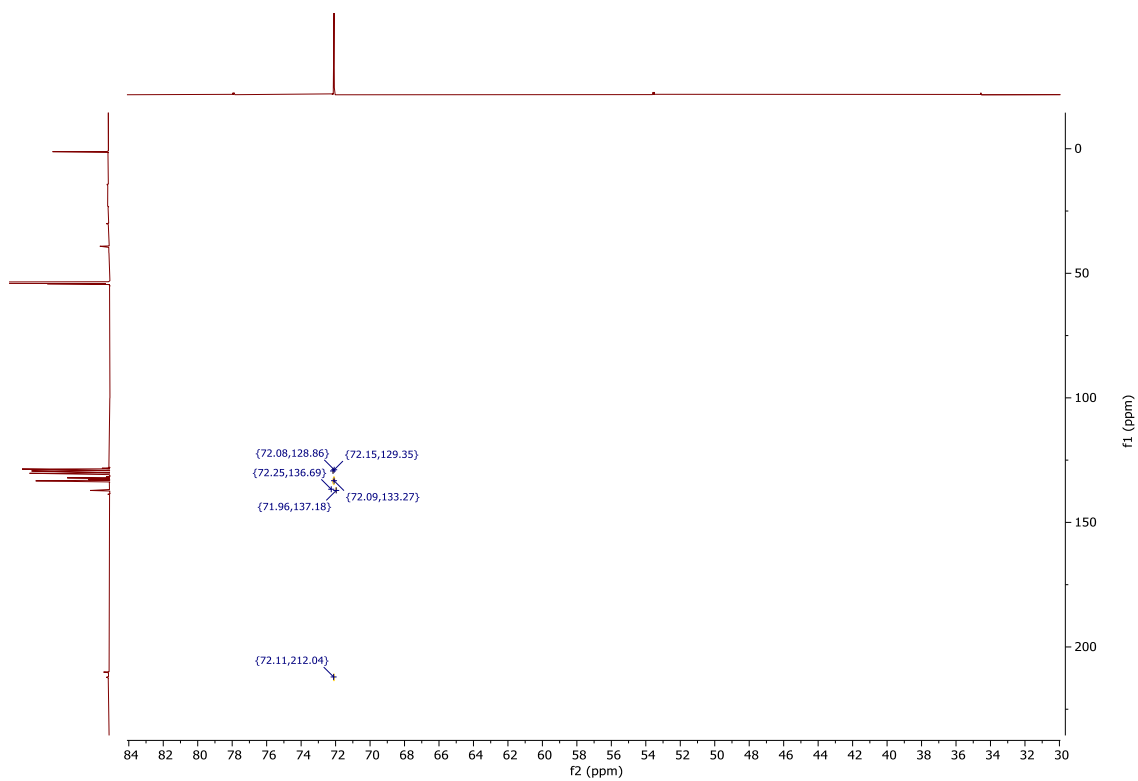


Figure 8: HMQC ^{31}P - $^{13}\text{C}\{^1\text{H}\}$ (10Hz) of compound **3**.

b. NMR spectra for compound **4**.

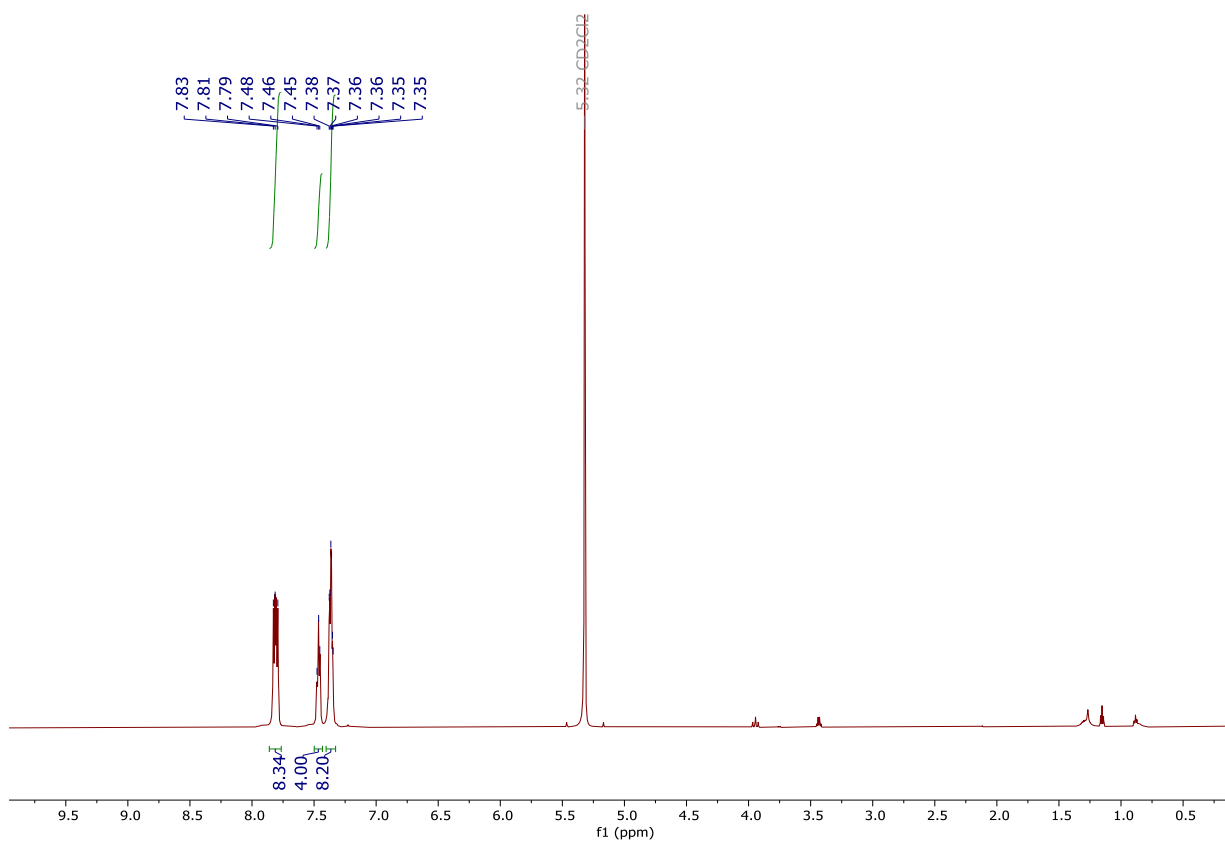


Figure 9: ^1H NMR spectrum of **4** in CD_2Cl_2 .

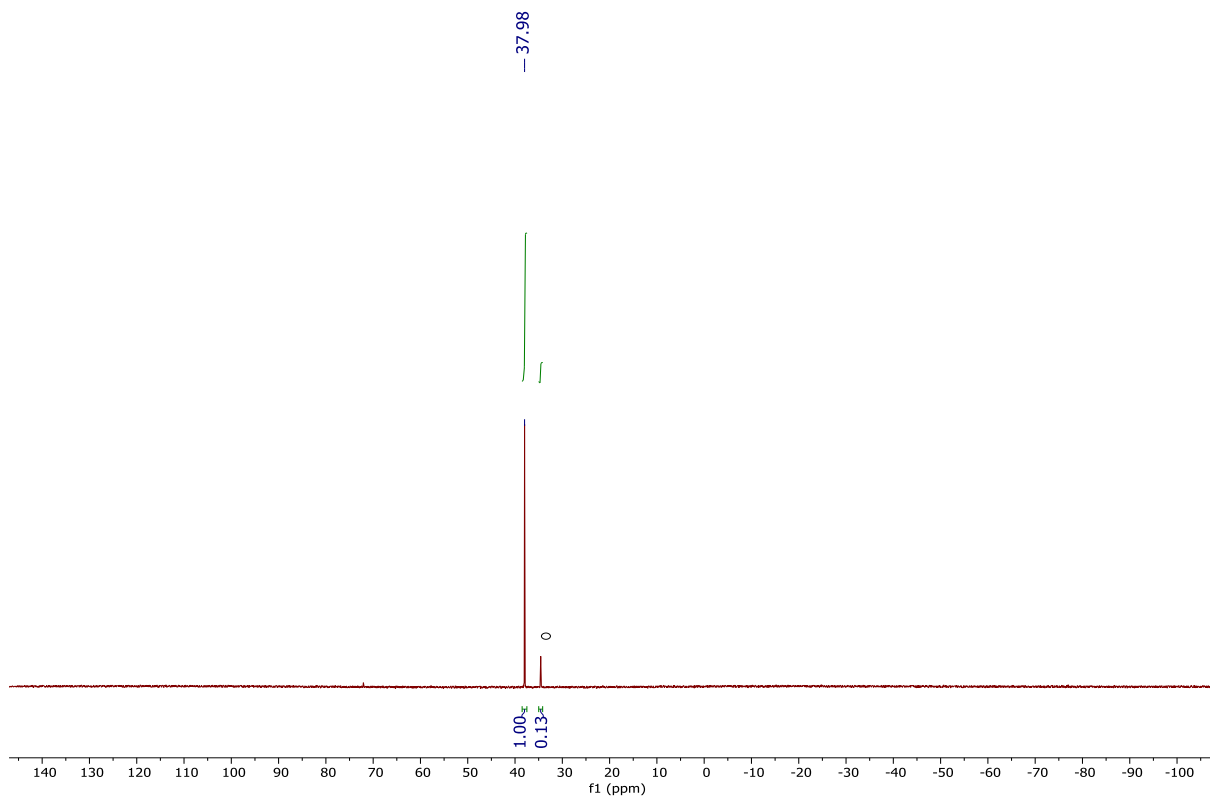


Figure 10: $^{31}\text{P}\{^1\text{H}\}$ NMR spectrum of **4** in CD_2Cl_2 . Circle: hydrolysis to $\{\text{Ph}_2\text{P}(\text{S})\}_2\text{CH}_2$.

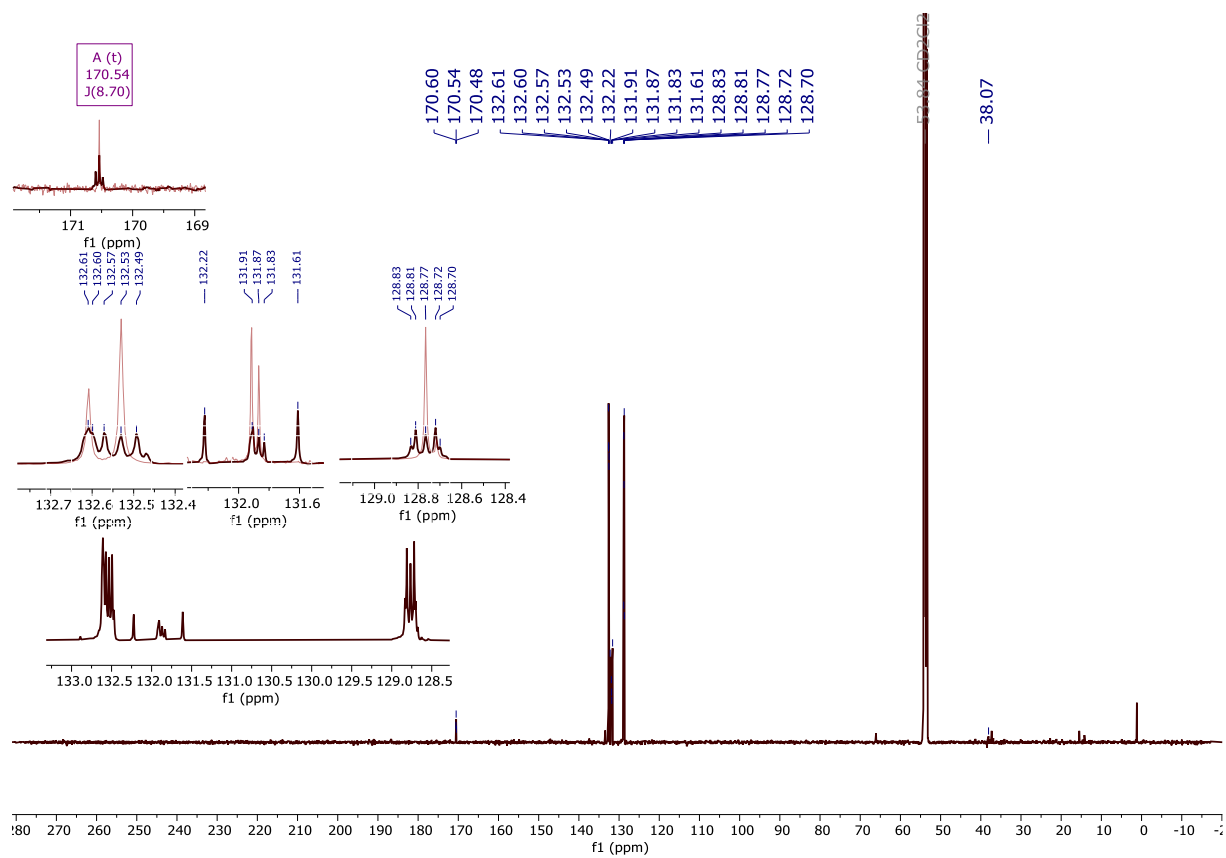


Figure 11: $^{13}\text{C}\{^1\text{H}\}$ NMR spectrum of **4** in CD_2Cl_2 . Insets: overlap of $^{13}\text{C}\{^1\text{H}\}$ and $^{13}\text{C}\{^{31}\text{P}\}\{^1\text{H}\}$ NMR.

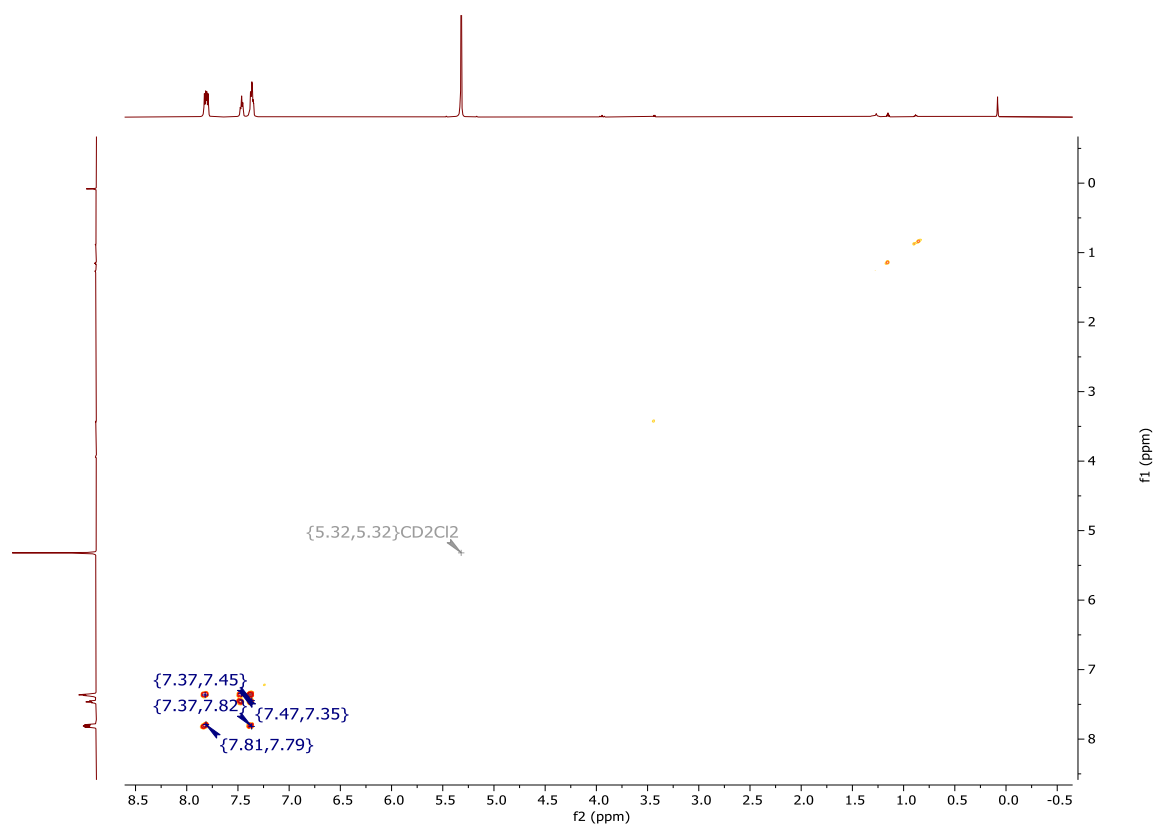


Figure 12: ^1H - ^1H COSY spectrum of 4 in CD_2Cl_2 .

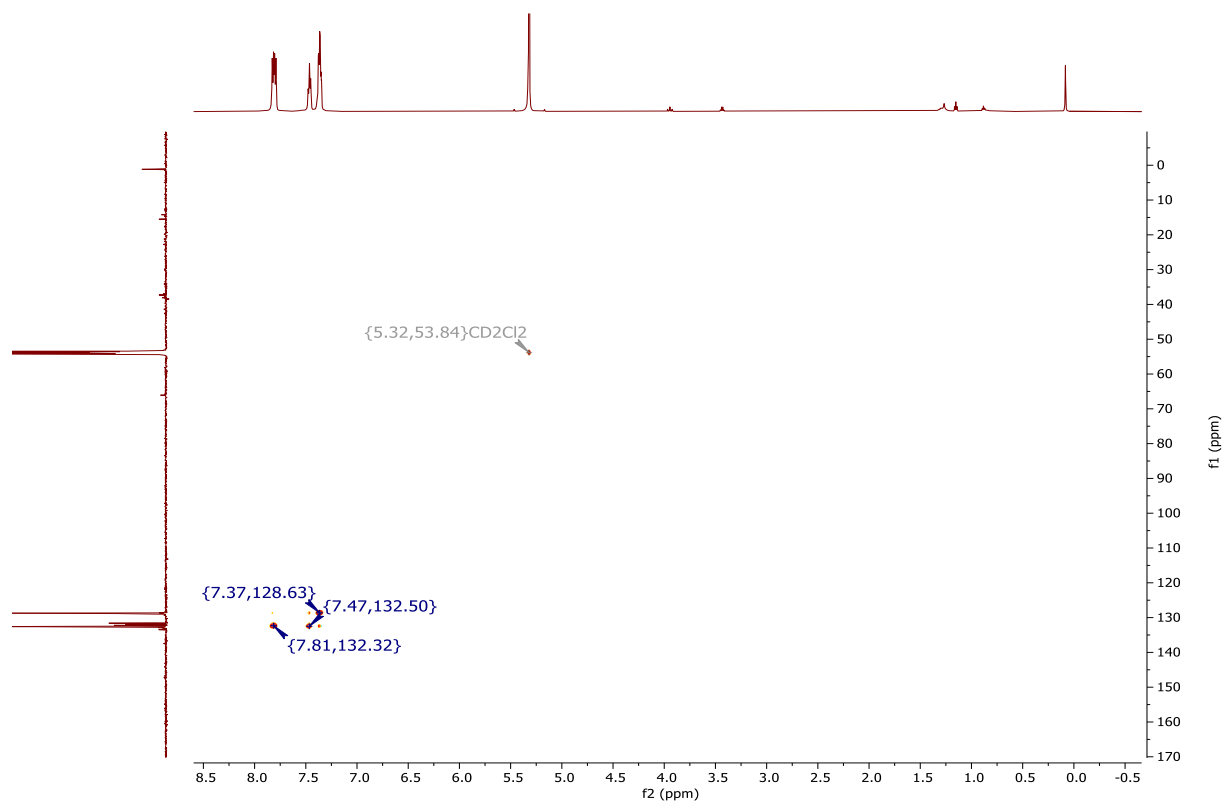


Figure 13: ^{13}C - ^1H HSQC spectrum of 4 in CD_2Cl_2 .

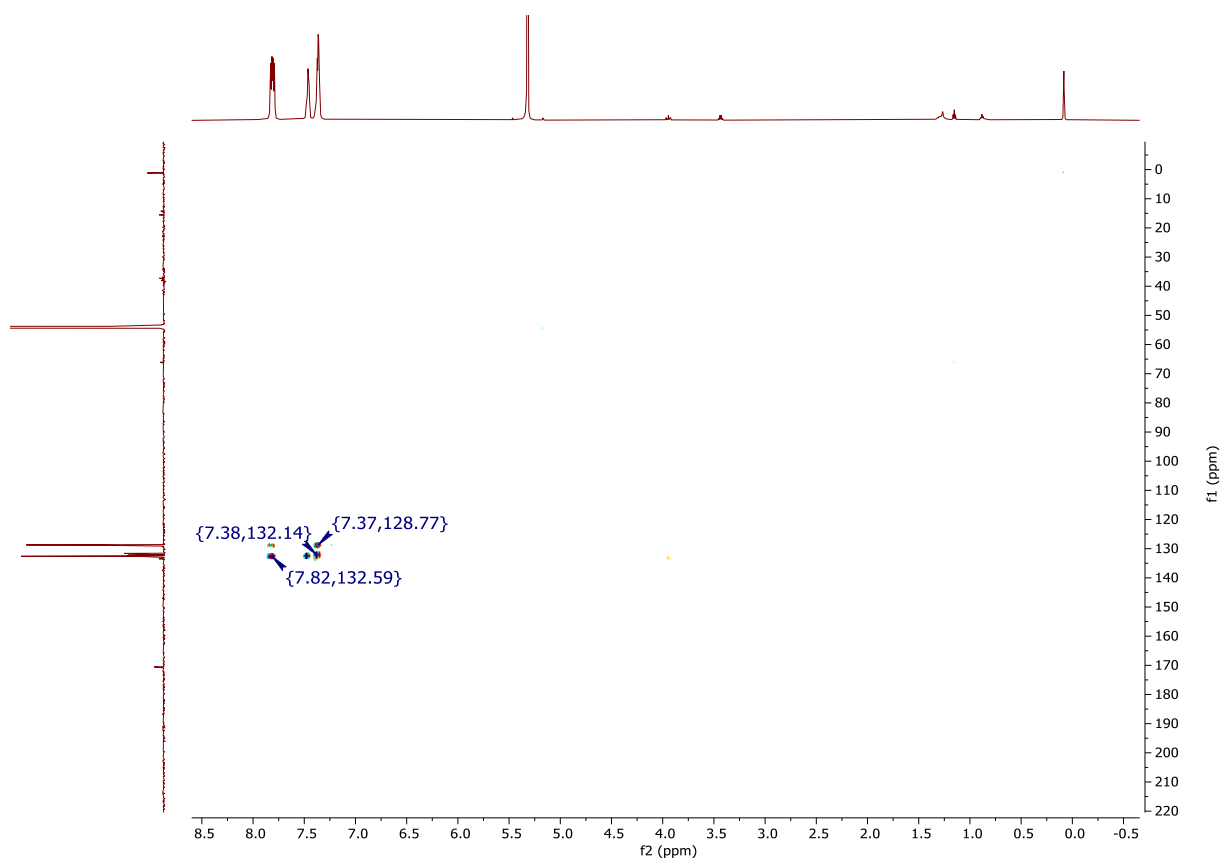


Figure 14: ^{13}C ^1H HMBC spectrum of **4** in CD_2Cl_2 .

c. NMR data for intermediate **A** at -40°C .

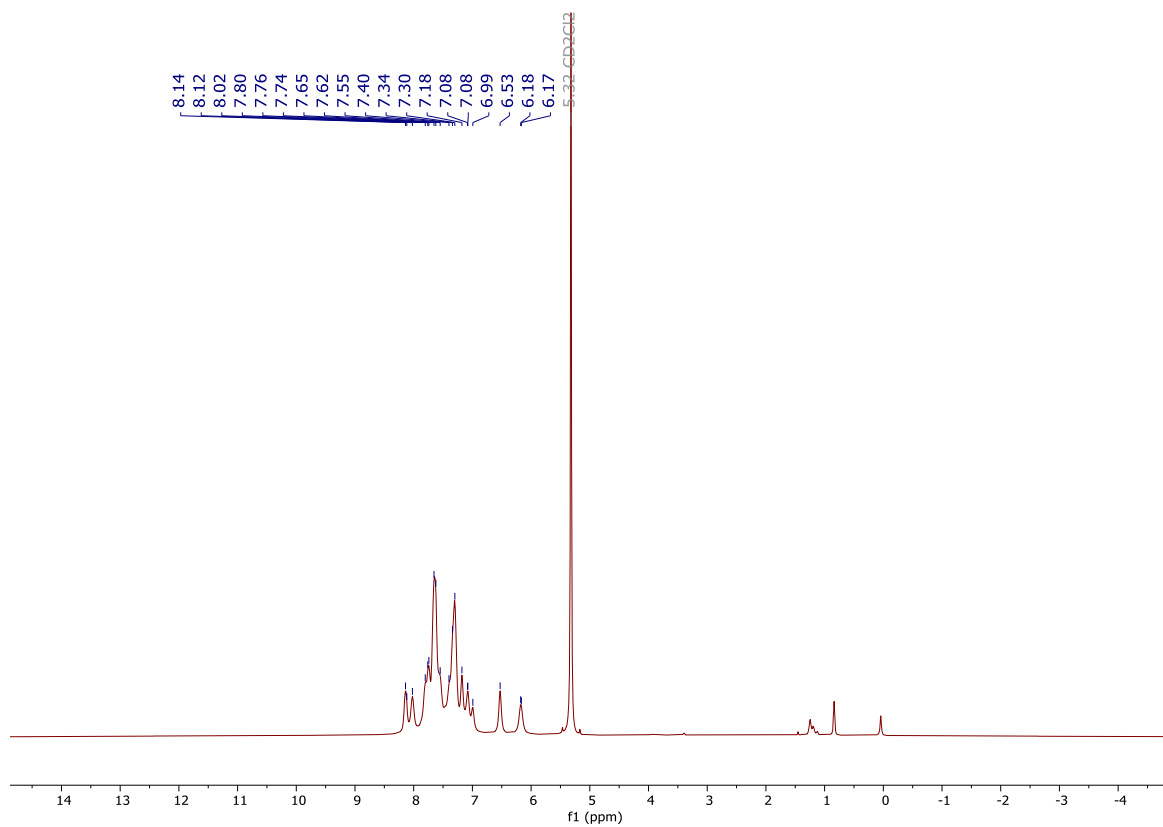


Figure 15: ^1H NMR of intermediate **A** in CD_2Cl_2 at -40°C .

MHT 2eme.154.fid
RRM0321 CD2Cl2 13C{1H} zgpg45 T=-40C

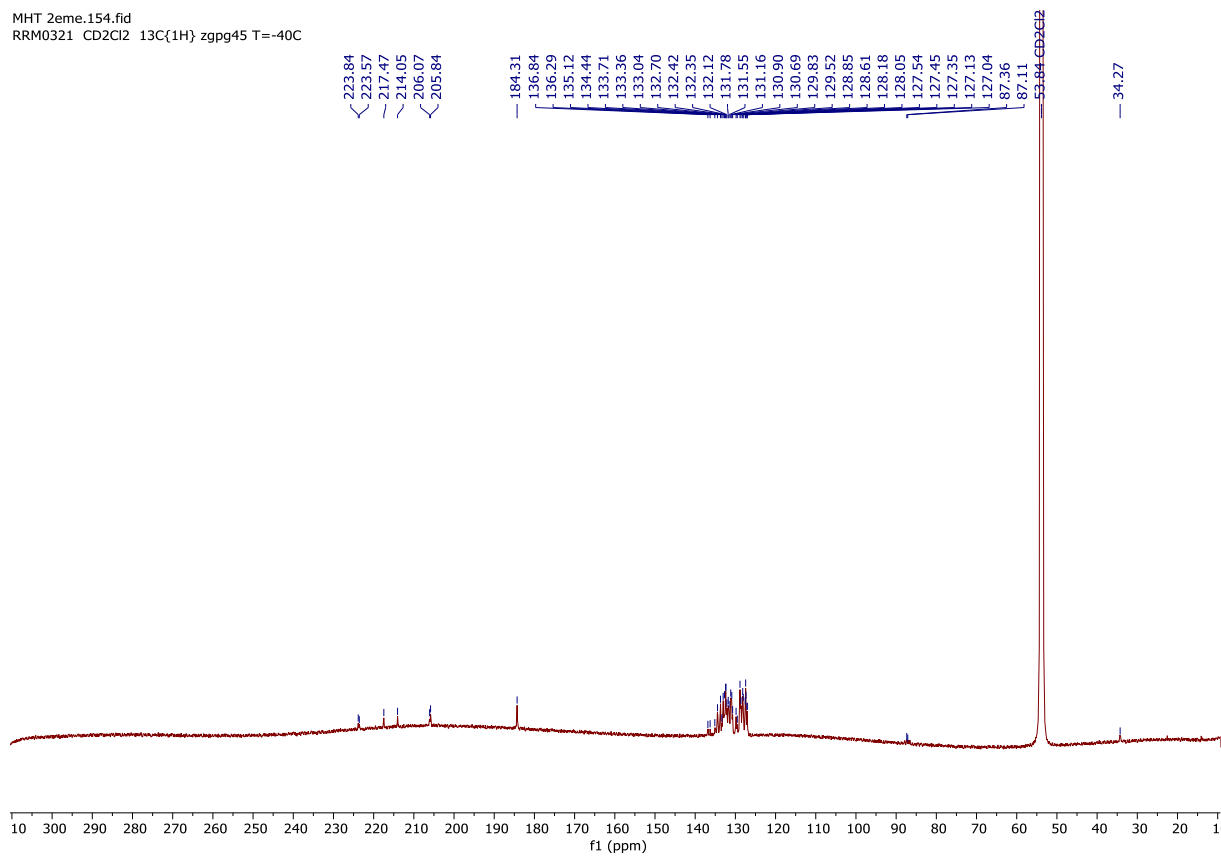


Figure 16: $^{13}\text{C}\{^1\text{H}\}$ NMR spectrum of intermediate **A** at -40°C in CD_2Cl_2 .

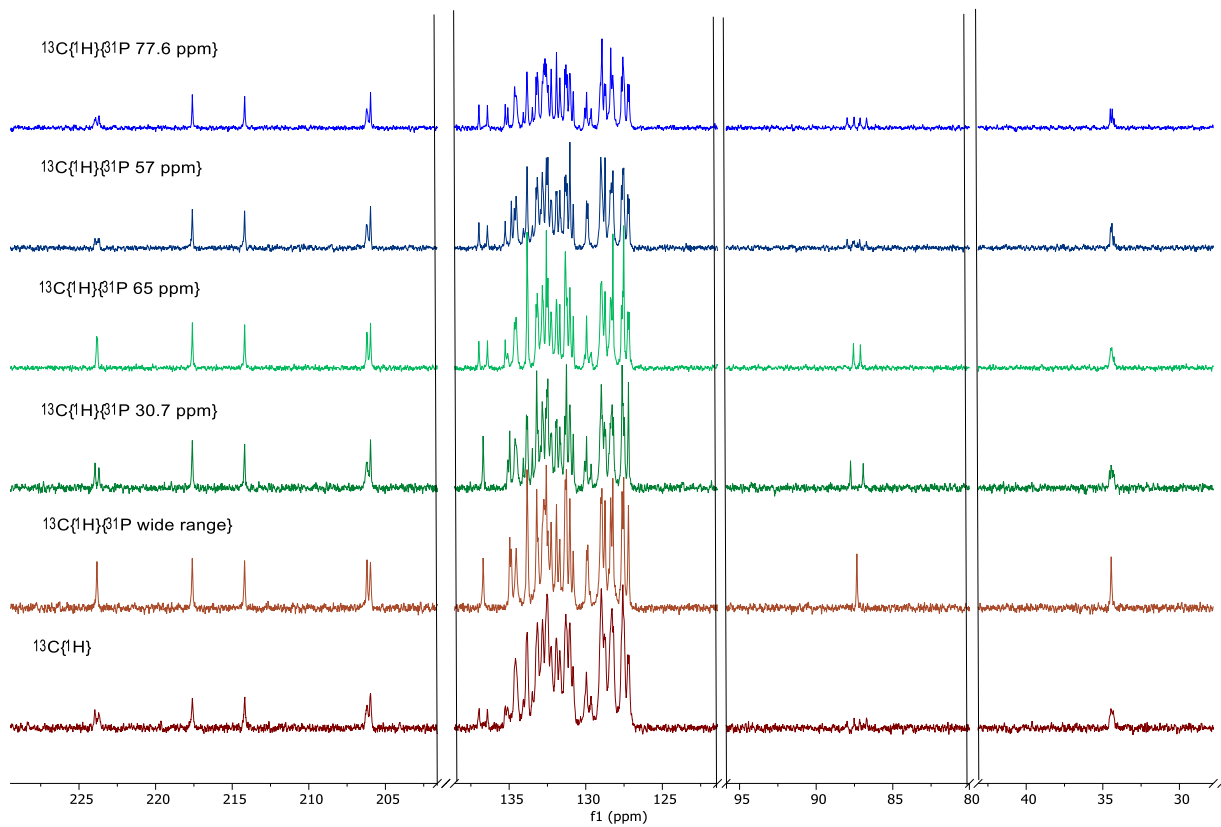


Figure 17: $^{13}\text{C}\{^1\text{H}\}$ NMR spectra of intermediate **A** (-40°C) with various (selective) ^{31}P decoupling.

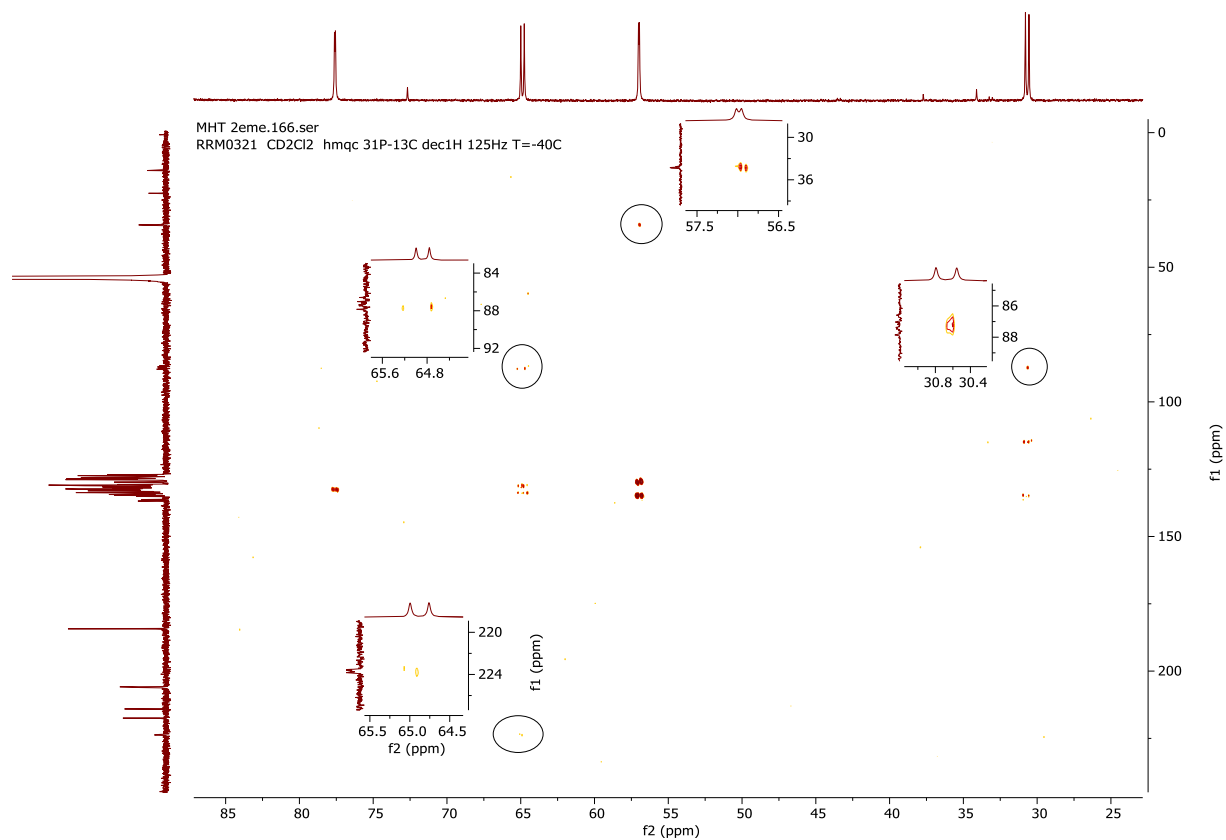


Figure 18: ^{31}P - ^{13}C HMQC ($J=125$ Hz) of intermediate **A** at -40°C .

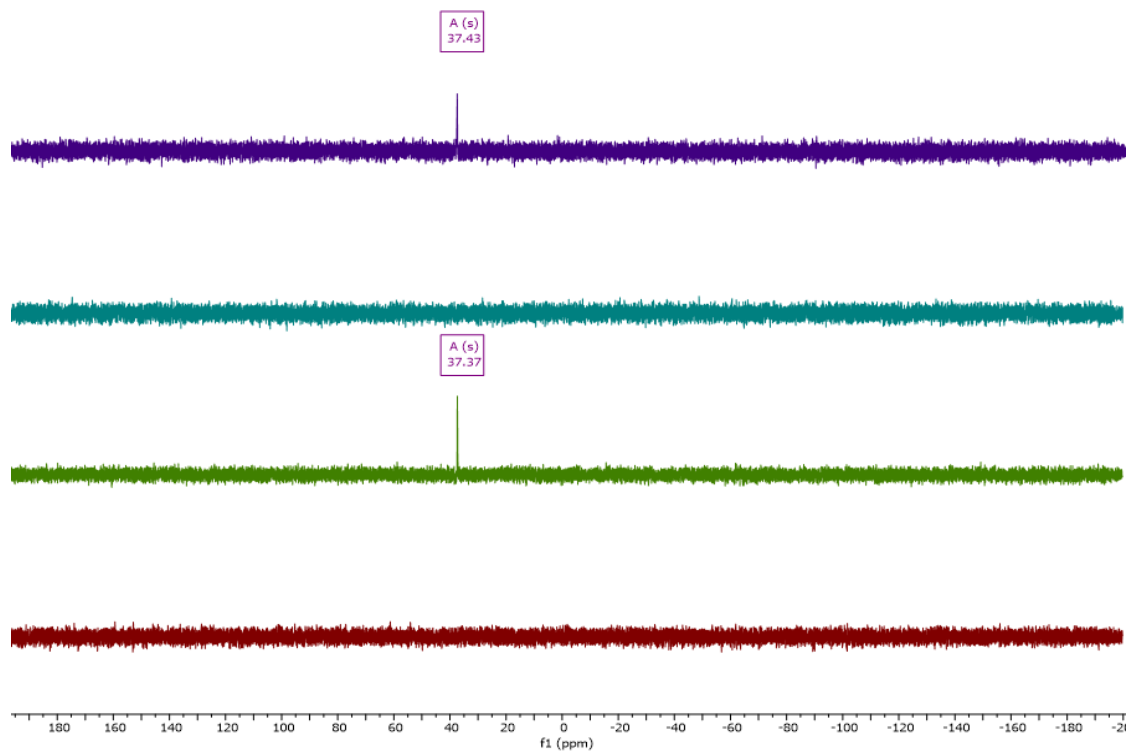
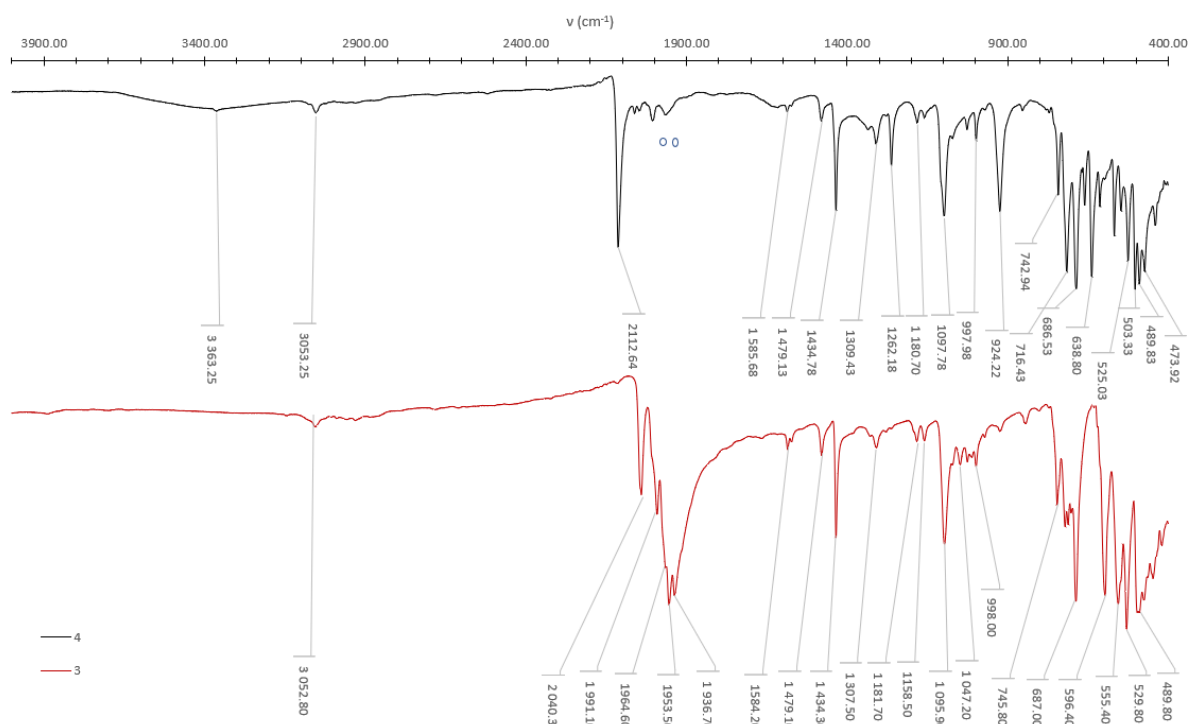


Figure 19: $^{31}\text{P}\{^1\text{H}\}$ NMR spectra showing the reversibility of the coordination of **4** on the unknown paramagnetic complex. From bottom to top, in the same tube: CD_2Cl_2 , THF-d^8 , CD_2Cl_2 , THF-d^8 . No precipitate was seen in CD_2Cl_2 .

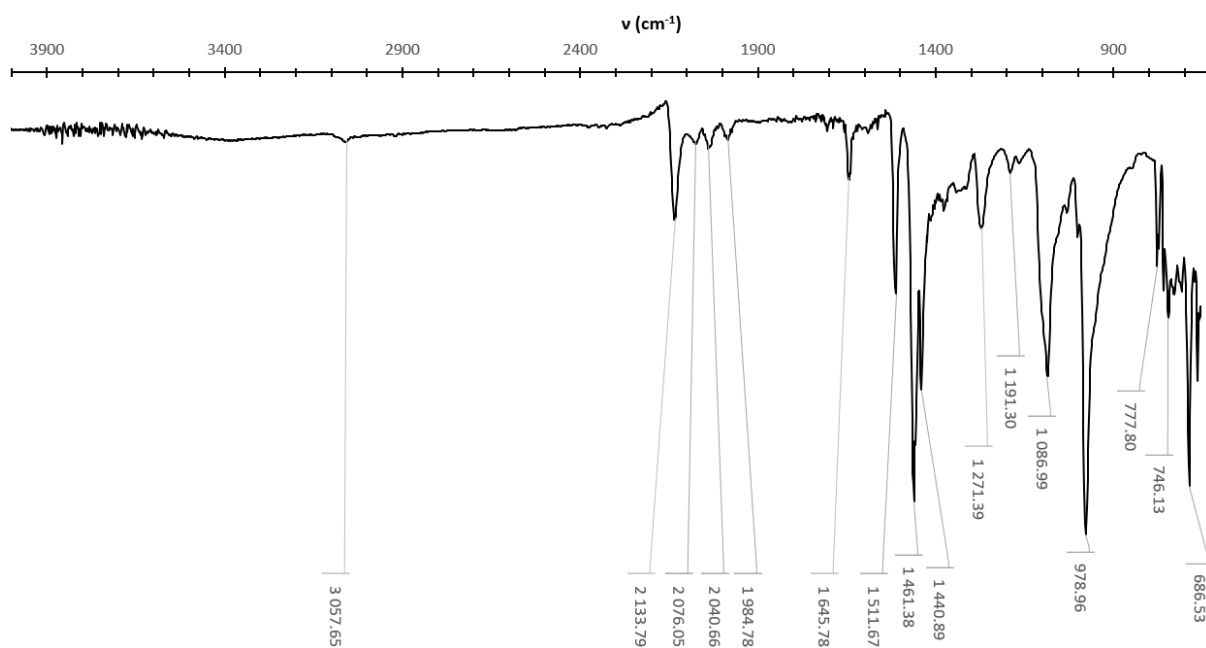
4. IR spectroscopy

a. IR spectra of **3** and **4**.

Circles represents absorption from impurities.

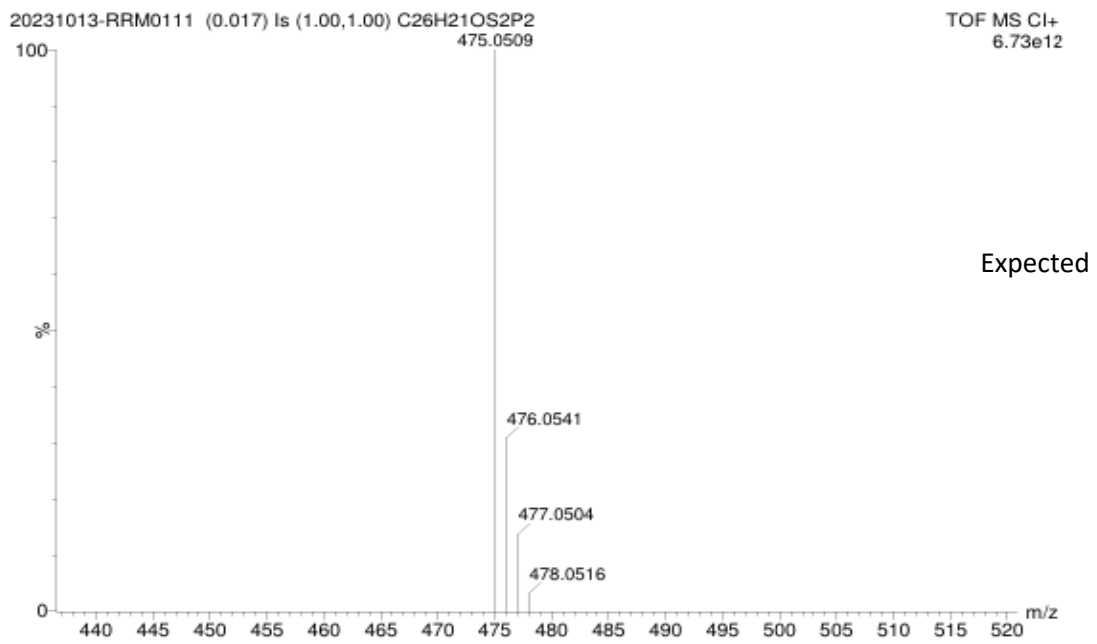
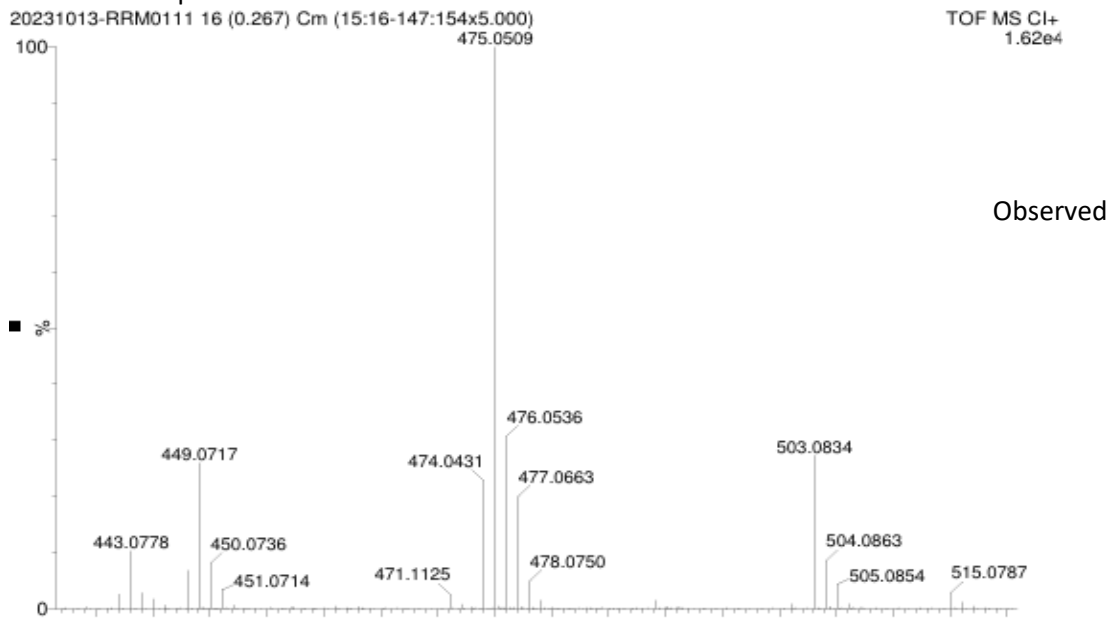


b. IR spectrum of the byproduct of the reaction between **3** and CO.

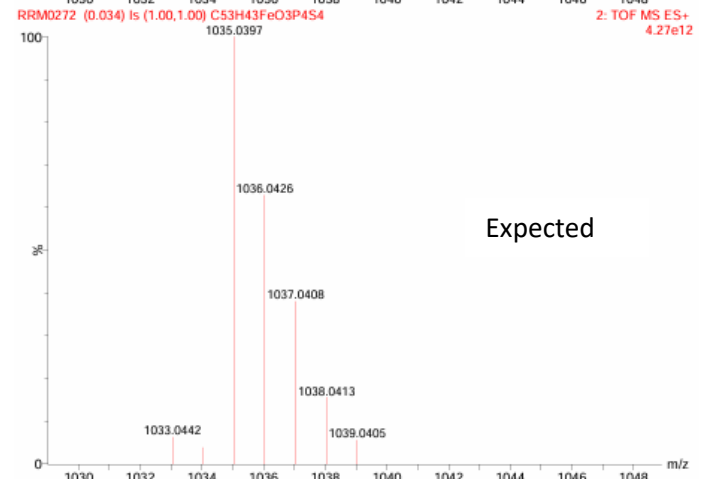
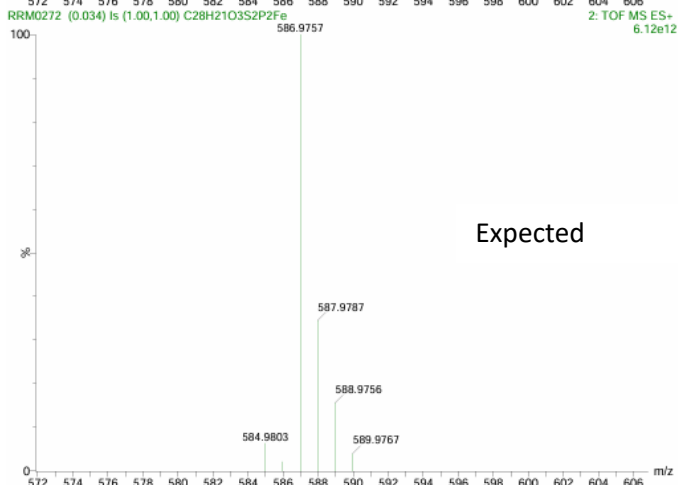
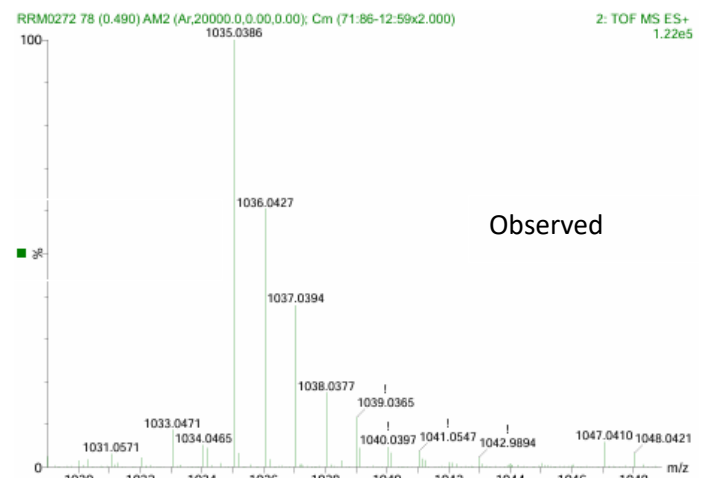
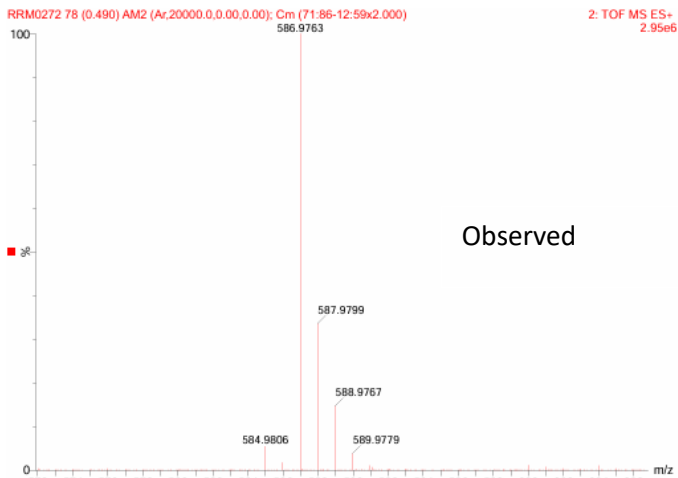
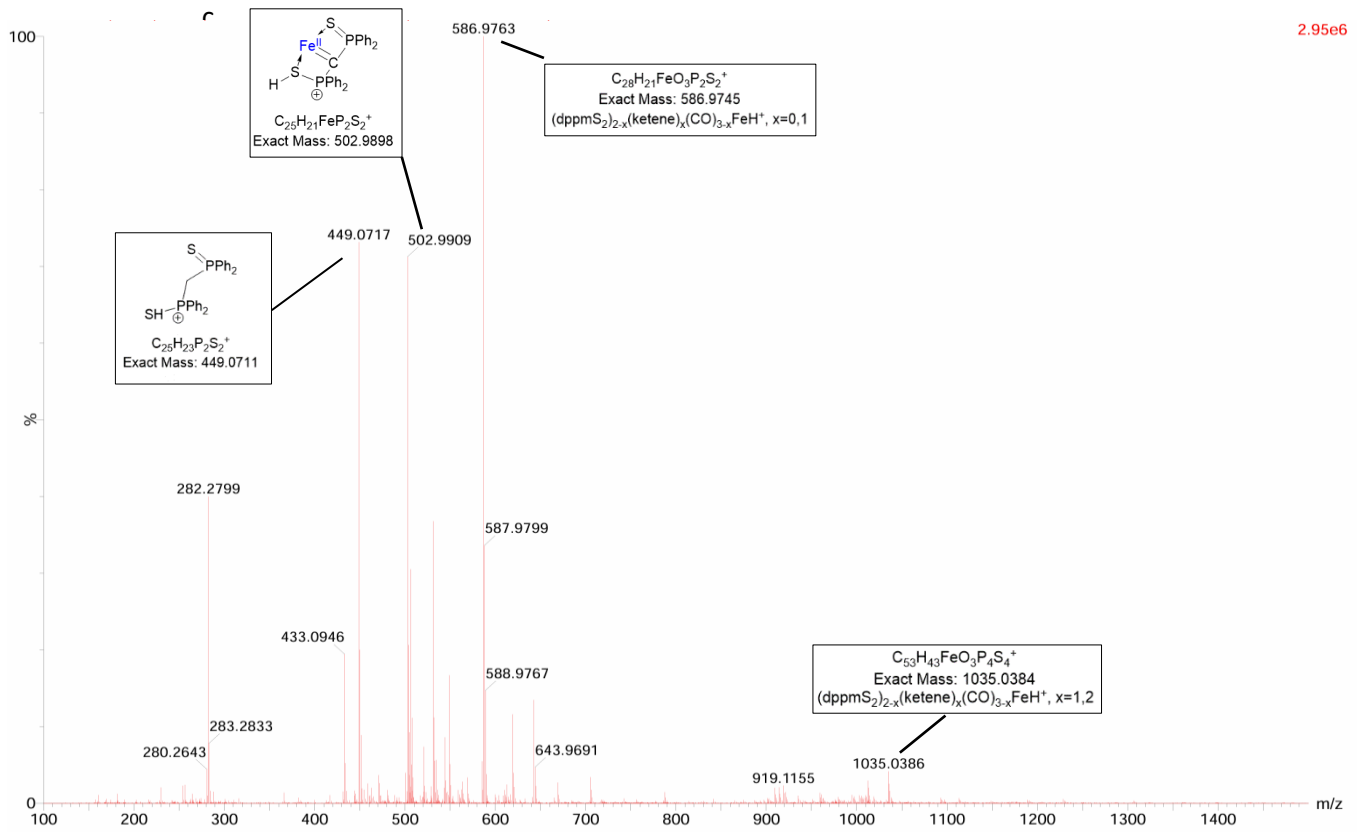


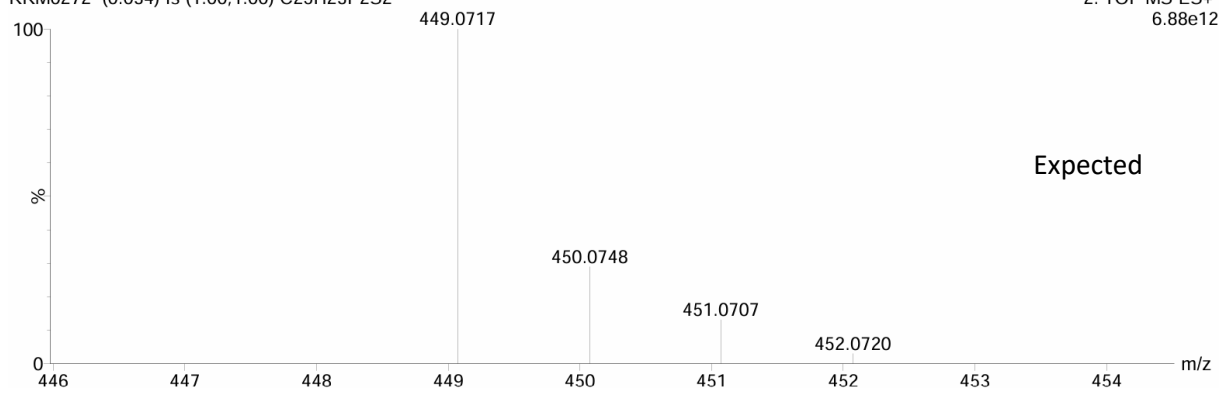
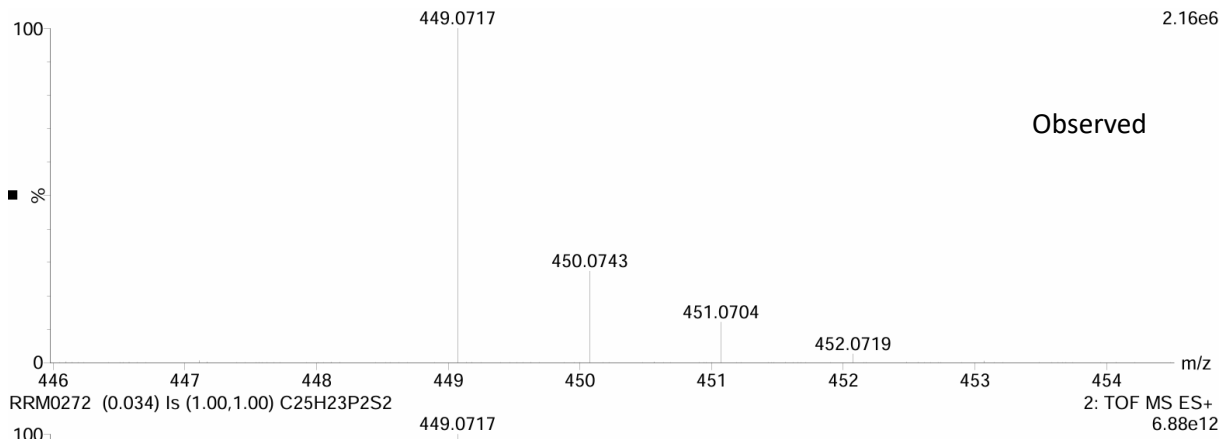
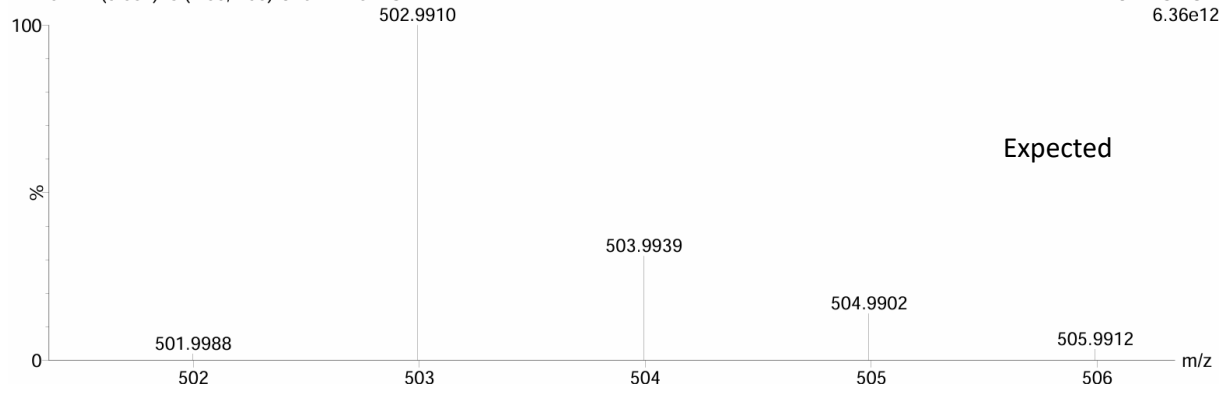
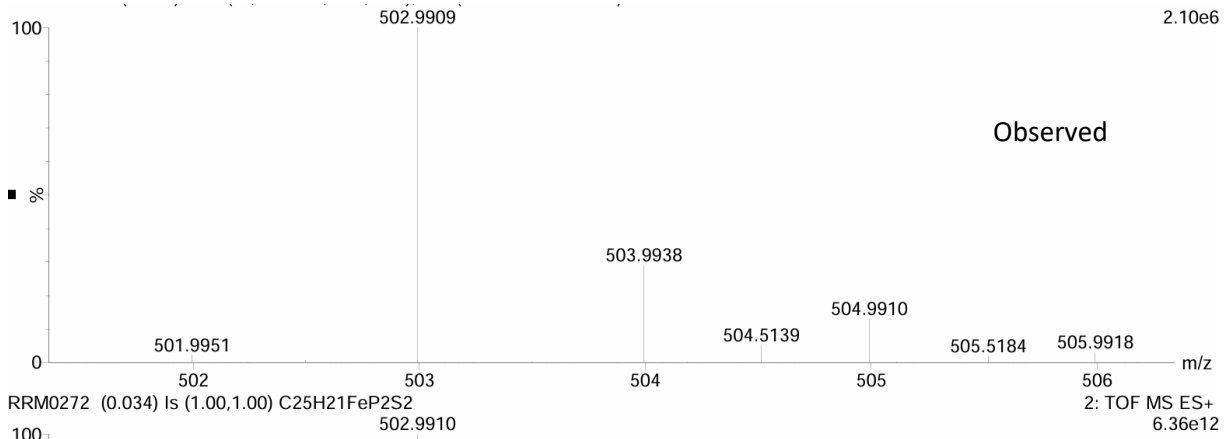
5. Mass spectroscopy

a. Compound 4



b. Byproduct of the reaction of 2 and CO.





6. X-ray diffraction

Table 1: Crystallographic details for compounds **3** and **4**

	Compound 3	Compound 4
Empirical formula	C ₃₁ H ₂₀ Fe ₂ O ₆ P ₂ S ₂	C ₂₆ H ₂₀ OP ₂ S ₂
Formula weight	726.23	474.48
Temperature	193(2) K	193(2) K
Wavelength	0.71073 Å	0.71073 Å
Crystal system	Triclinic	Monoclinic
Space group	<i>P</i> $\bar{1}$	<i>C</i> 2/ <i>c</i>
a (Å)	12.259(3)	24.929(3)
b (Å)	15.825(3)	9.3898(12)
c (Å)	16.510(4)	21.714(3)
α (°)	86.072(5)	90
β (°)	71.586(5)	112.245(3)
γ (°)	89.707(5)	90
Volume (Å ³)	3031.1(11)	4704.4(10)
Z	4	8
Density (calculated)	1.591 mg/m ³	1.340 mg/m ³
Absorption coefficient	1.244 mm ⁻¹	0.379 mm ⁻¹
F(000)	1472	1968
Crystal size (mm ³)	0.060 x 0.050 x 0.040	0.160 x 0.050 x 0.030
Theta range for data collection	1.290 to 24.815°	2.027 to 26.369°
Reflections collected	81304	80799
Independent reflections	10431 [R(int) = 0.1682]	4822 [R(int) = 0.1424]
Completeness	99.5 %	99.9 %
Data / restraints / parameters	10431 / 0 / 775	4822 / 0 / 280
Goodness-of-fit on F ²	1.071	1.032
Final R indices [I>2σ(I)]	R1 = 0.0823, wR2 = 0.1606	R1 = 0.0614, wR2 = 0.1360
R indices (all data)	R1 = 0.1648, wR2 = 0.1938	R1 = 0.1173, wR2 = 0.1646
Largest diff. peak and hole	0.896 and -0.641 e.Å ⁻³	0.699 and -0.481 e.Å ⁻³
CCDC number	2424974	2424975

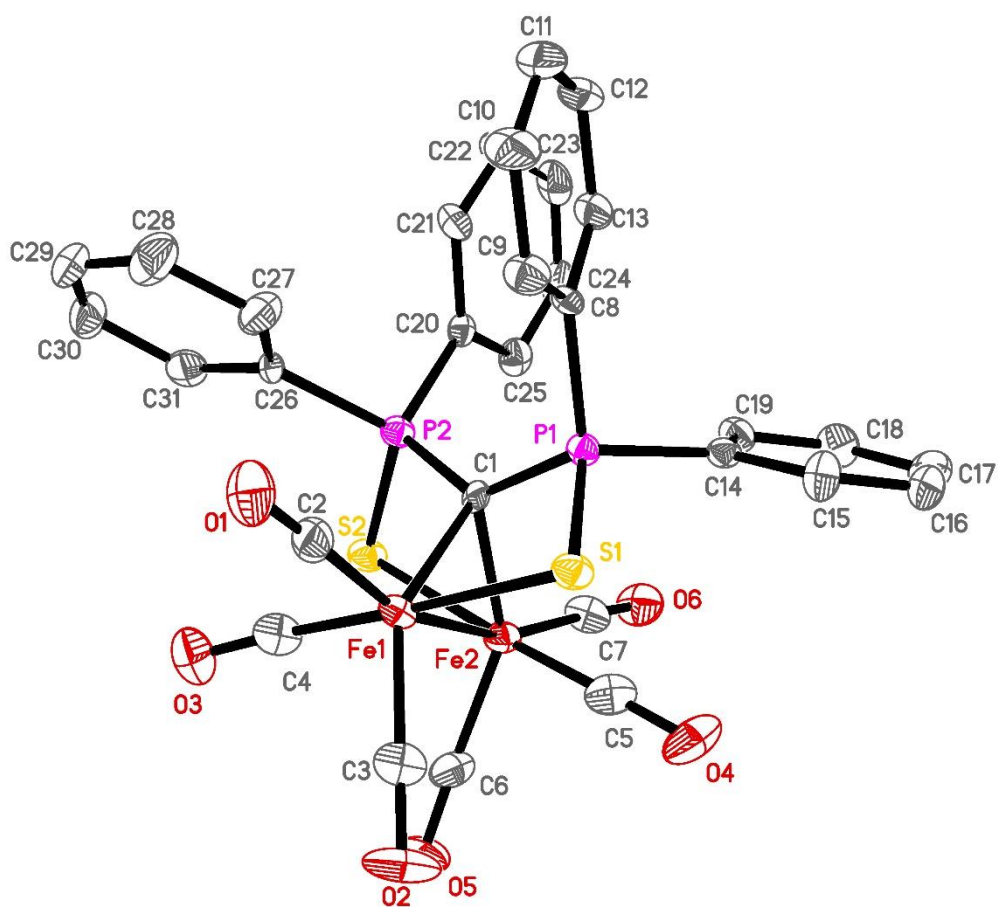


Figure 20: Molecular structure of compound **3**. Thermal ellipsoids are represented at 30% probability level. For clarity H atoms are omitted and only one of the two independent molecules of the asymmetric unit is shown.

Table S2: Selected bond lengths (Å) and angles (°) for complex **3**.

Fe1-C1	2.046(8)	Fe2-C1	2.032(9)
Fe1-C2	1.782(12)	Fe2-C7	1.788(11)
Fe1-C3	1.794(11)	Fe2-C6	1.794(11)
Fe1-C4	1.740(11)	Fe2-C5	1.736(12)
Fe1-S1	2.408(3)	Fe2-S2	2.415(3)
Fe1-Fe2	2.626(2)		
P1-C1	1.763(9)	P2-C1	1.736(9)
P1-S1	2.005(3)	P2-S2	2.008(3)
P2-C1-P1	133.5(5)	P1-C1-Fe1	96.4(4)

Fe2-C1-Fe1	80.2(3)	P2-C1-Fe1	119.1(4)
C1-Fe1-Fe2	49.7(2)	P1-C1-Fe2	117.9(4)
C1-Fe2-Fe1	50.1(2)	P2-C1-Fe2	98.3(4)
C2-Fe1-Fe2	159.5(3)	C4-Fe1-S1	177.8(4)
C7-Fe2-Fe1	160.8(3)	C5-Fe2-S2	177.0(4)
C3-Fe1-C1	143.6(4)	C6-Fe2-C1	144.1(4)

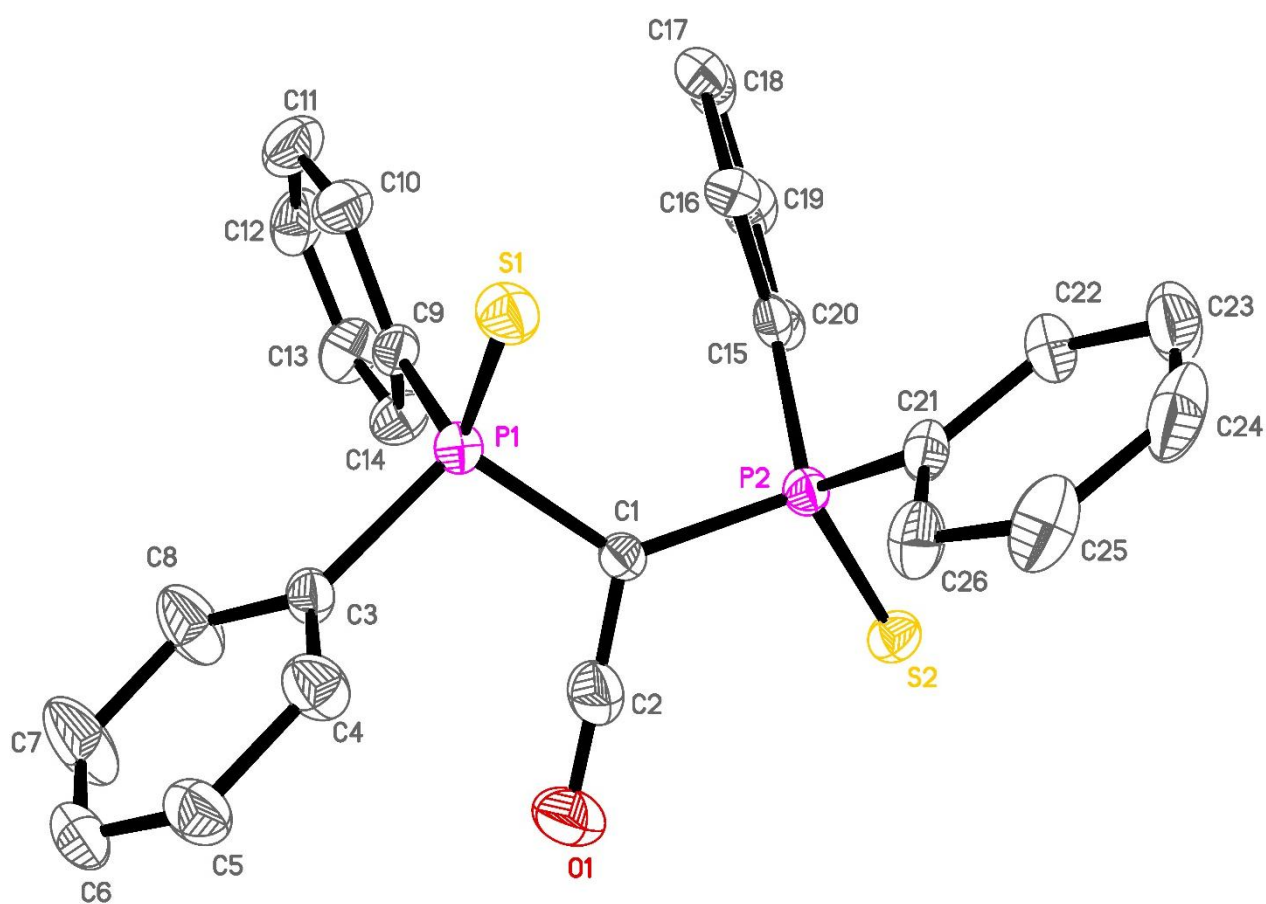


Figure 21: Molecular structure of compound **4**. Thermal ellipsoids are represented at 30% probability level. H atoms are omitted for clarity.

Table S3: selected bond lengths (Å) and angles (°) for compound **4**.

O1-C2	1.184(6)	P2-S2	1.9509(15)
C1-C2	1.280(6)	P1-C3	1.813(4)

C1-P1	1.818(4)	P1-C9	1.811(4)
C1-P2	1.801(4)	P2-C15	1.809(4)
P1-S1	1.9480(15)	P2-C21	1.808(4)
P1-C1-C2	115.9(3)	O1-C2-C1	179.0(5)
P2-C1-C2	114.8(3)	C1-P1-S1	112.7(1)
P2-C1-P1	128.8(2)	C1-P2-S2	109.4(1)

7. Mössbauer spectroscopy
a. Compound **3**

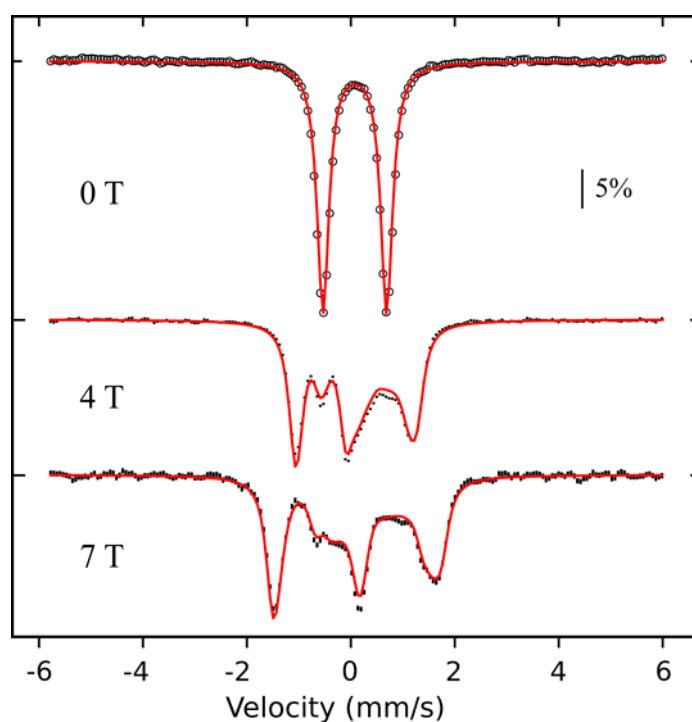


Figure 22: Mössbauer spectra recorded at 5.6 K in variable magnetic fields applied parallel to the gamma-rays. The black circles and error bars represent the experimental data, while the red solid lines are the $S = 0$ spin-Hamiltonian simulations with the following parameters: $\delta = 0.07$ mm/s, $\Delta E_Q = 1.23$ mm/s, $\eta = 0.27$, $\Gamma = 0.26$ mm/s.

b. Iron-containing byproduct of the reaction between **2** and CO

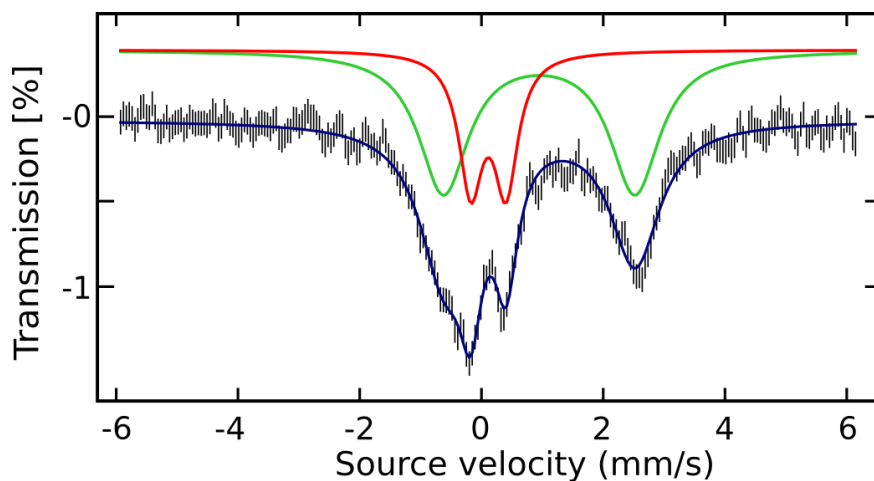


Figure 23: Mössbauer spectra recorded at 5.7 K in a 600 G magnetic field applied parallel to the gamma-rays. The black error bars represent the experimental data, while the colored solid lines are quadrupole doublet simulations. The green line, accounting for 69% of total Fe, featuring large values of δ (0.95 mm/s), ΔE_Q (3.14 mm/s) and Γ (0.99 mm/s), is assigned to adventitiously-bound Fe^{II}. The red line, accounting for 31% of total Fe, displays a small isomer shift ($\delta = 0.11$ mm/s, $\Delta E_Q = 0.58$ mm/s, $\Gamma = 0.47$ mm/s) and is assigned to an Fe^I-carbonyl species.

8. Computational details

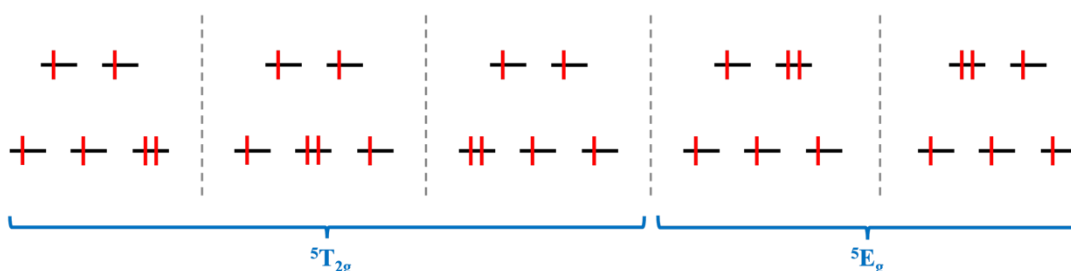
Ab initio calculations were performed on complex **1** to address the question of the spin multiplicity of the Fe^{II} ions and the low-energy spectrum of the complex.

The X-ray structure was used except for the position of the H atoms which were optimized by DFT calculations (with the PBE exchange-correlation functional and the D3(BJ) dispersion correction) using def2-SVP atomic basis sets (5s3p2d1f for Fe, 4s3p1d for P and S, 3s2p1d for C and 2s1p for H).

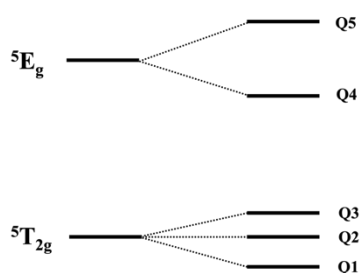
Wave function based calculations (CASSCF and NEVPT2) were also performed to shed some light on the low energy spectrum and wave functions.

Local d-d excitation energies are estimated from CAS(6,5)SCF calculations (with 6 active electrons in 5 active orbitals) performed on a complex where one of the two Fe^{II} is substituted by a diamagnetic Zn^{II} ion.⁷ The ground quintet state (Q1) is well separated from the states of the other spin multiplicities of the d⁵ configuration, the lowest triplet and singlet states being at the CASCI level at ≈ 18000 and ≈ 24000 cm⁻¹, respectively, definitely confirming the high spin character of the Fe(II) ions. Moreover, Q1 is mainly single configurational (*i.e.* one of the 3d MO is almost doubly occupied while the 4 others are singly occupied). The Q2-Q5 excited quintet states are at 555, 878, 4605 and 5793 cm⁻¹, respectively, in the one case, and 883, 1115, 4530 and 6240 cm⁻¹, respectively, in the other case. This means that at low temperature, these local excited states cannot be populated and thus cannot be key for the magnetism of this compound. However, it is clear that two to three quintet states are within 1000 cm⁻¹, and that this near-orbital degeneracy (triple) may deserve a further theoretical study.

The five high-spin d⁵ configurations and their involvement the S=2 many-electron states in the O_h symmetry point group:

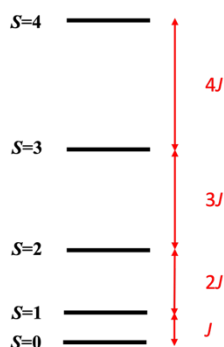


Schematic representation of the energies of the S = 2 many-electron states in the O_h symmetry point group and in the substituted complexes:



Assuming that locally only a single configurational Q1 is at play, CAS(8,8)SCF+NEVPT2 calculations were performed to evaluate the coupling between the local ground state of each Fe(II) ions in complex **1**. The ground state is a singlet state, indicating an antiferromagnetic coupling between the two local quintet states. At the CASSCF level, using state average MOs, the energy spectrum follow almost perfectly the gaps predicted by an Heisenberg Hamiltonian model ($\mathbf{H} = -J \mathbf{S}_i \cdot \mathbf{S}_j$) with a coupling constant $J = -87$ cm⁻¹: $E(S=1) = 87$ cm⁻¹, $E(S=2) = 262$ cm⁻¹, $E(S=3) = 522$ cm⁻¹ and $E(S=4) = 867$ cm⁻¹, compared to the ground state.

Schematic representation of the successive Heisenberg energy gaps for antiferromagnetically coupled high-spin Fe^{II} centers:

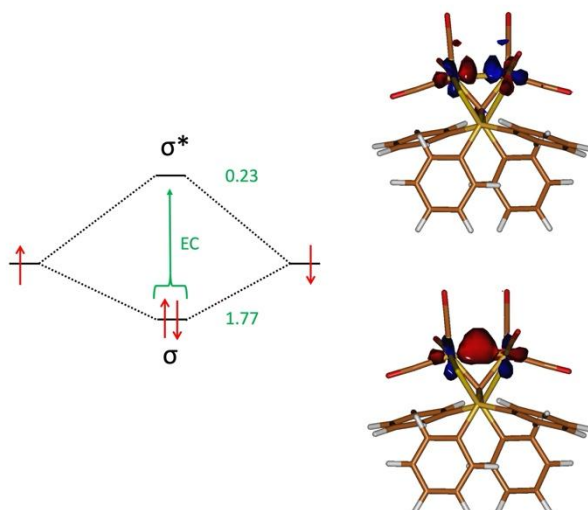


CAS(8,8)SCF calculations performed on state specific MOs confirm the antiferromagnetic coupling, but, as expected, lead to a less perfect Heisenberg spectrum: $E(S=1) = 105 \text{ cm}^{-1}$, $E(S=2) = 299 \text{ cm}^{-1}$, $E(S=3) = 556 \text{ cm}^{-1}$ and $E(S=4) = 844 \text{ cm}^{-1}$. As expected, dynamic electron correlation enhances the antiferromagnetic character of the coupling, multiplying by almost 2 most of the energy gaps at the NEVPT2 level.

These calculations were corroborated by CAS(12,10)SCF+NEVPT2 calculations. The CAS(12,10)SCF spectrum is in line with the CAS(8,8)SCF one (0, 111, 328, 605 and 919 cm^{-1} , respectively) while NEVPT2 predicts $J = -176 \text{ cm}^{-1}$ if we consider the $S=0 \leftrightarrow S=4$ energy gap.

Def2-TZVP atomic basis sets were used for Fe and Zn ions, and the atoms of their coordination sphere (6s4p4d1f for Fe and Zn, 5s5p2d1f for S and 5s3p2d1f for C) and def2-SVP for other atoms. All calculations were performed using the Orca 5 suite of programs.

For complex **3**, CAS(2/2)SCF calculations were performed with a similar computational setup as above. Two calculations were performed, a state-average calculation with one singlet and one triplet state to compute the singlet to triplet energy gap, and a state-specific calculation for the ground singlet state to interpret its wave function with the effective bond order perspective.⁸ The two active orbitals are in both cases the metal-metal σ and σ^* orbitals. The singlet to triplet energy gap being $\approx 5700 \text{ cm}^{-1}$, it was clear that this complex was not to be described with a Heisenberg Hamiltonian. We indeed suspected a single bond between the metals, hence the effective bond order determination. The occupation of the (natural) σ and σ^* orbitals being 1.77 and 0.23, respectively, an effective bond order of 0.77 is found. The deviation of the effective bond order from the formal one is a simple correlation effect, as in H_2 , associated with the double σ to σ^* excitation, leading to the contributions of both the σ^2 (88.4%) and σ^{*2} (11.5%) determinants in the (multiconfigurational) ground-state wave function. If one electron is removed, as it would be the case in any putative Fe^{II}Fe^I complex derived from **3**, the Brillouin theorem would block any excitation from the ground orbital configuration, meaning that the effective bond order would simply equal the formal one of 0.5.



We have also performed some preliminary DFT calculations to compare the different reactivities of an Fe^IFe^I model complex vs. an even more putative Fe^IFe^{II} one. The model complexes have been derived from **3** by substituting a CO ligand by a simple H₂C=C=O ketene one. Without performing a full conformational analysis, we have determined the geometries of various conformers and compared cases with similar conformers for both situations. For comparison purposes, we have imagined the following reaction:



Note that in the Fe^IFe^I case, the final complex is directly **3**. We have determined only pure electronic energies. All the model reactions were found exothermic, meaning that the ketene H₂C=C=O would be released in all the cases. More importantly, we found two main differences between the Fe^IFe^I and Fe^IFe^{II} cases:

- In each case, our model reaction is much more exothermic in the Fe^IFe^I case than in the Fe^IFe^{II} one. Comparable reaction energies can be for instance -97 kJ/mol in the Fe^IFe^I case and -55 kJ/mol in the Fe^IFe^{II} one. This means that potential precursors of **3** are highly keen to release ketenes, leading in our case to the easy formation of **3**.
- In the Fe^IFe^{II} case, the initial complex displays localized valences, the ketene being bound to the Fe^{II} site, while the final complex is valence delocalized. This is in line with the idea that ketenes have more affinity for Fe^{II} ions vs. Fe^I.

All-in-all, this leads us to the statement that is reported in the main text: "From this study, we confirm that ketenes have a better affinity for Fe^IFe^{II} complexes than for Fe^IFe^I ones. Note that while the ketene binds on localized Fe^{II} sites in the initial Fe^IFe^{II} complex, the final Fe^IFe^{II} complex is valence delocalized; the ketene thus acts as a "localization enforcer"."

For these calculations, the geometries of all the species were optimized with the B3PW91 exchange-correlation functional, with def2-TZVP atomic basis sets on all the atoms, and with the D3(BJ) dispersion correction, still with Orca 5.

9. References

- (1) Ravel-Massol, R.; Munshi, S.; Pujol, A.; Garcia-Serres, R.; Saffon-Merceron, N.; Mézailles, N.; Fustier-Boutignon, M. One Ligand to Bind Them All: S C S₂– Carbon- and Sulfur-Based Gem-Dianion as Structuring Ligand for Iron Polymetallic Assemblies. *Chemistry – A European Journal* **2023**, *29* (58), e202302130. <https://doi.org/10.1002/chem.202302130>.
- (2) SAINT, Program for Data Reduction (Bruker-AXS).
- (3) SADABS, Program for Data Correction (Bruker-AXS).
- (4) Sheldrick, G. M. SHELXT – Integrated Space-Group and Crystal-Structure Determination. *Acta Cryst A* **2015**, *71* (1), 3–8. <https://doi.org/10.1107/S2053273314026370>.
- (5) Sheldrick, G. M. Crystal Structure Refinement with SHELXL. *Acta Cryst C* **2015**, *71* (1), 3–8. <https://doi.org/10.1107/S2053229614024218>.
- (6) Garcia-Serres, R. easyMoss : A Python / PyQt5 User-Friendly Application for the Simulation of Mössbauer Spectra, 2021. <https://doi.org/10.5281/zenodo.5634948>.
- (7) Sergentu, D.-C.; Guennic, B. L.; Maurice, R. The Resolution of the Weak-Exchange Limit Made Rigorous, Simple and General in Binuclear Complexes. *Phys. Chem. Chem. Phys.* **2024**, *26* (8), 6844–6861. <https://doi.org/10.1039/D3CP04943D>.
- (8) Roos, B. O.; Borin, A. C.; Gagliardi, L. Reaching the Maximum Multiplicity of the Covalent Chemical Bond. *Angewandte Chemie International Edition* **2007**, *46* (9), 1469–1472. <https://doi.org/10.1002/anie.200603600>.